A pseudospectral method for the simulation of 3-D ultrasonic and seismic waves in heterogeneous poroelastic borehole environments

Rolf Sidler,[1,*] José M. Carcione[2] and Klaus Holliger[1]

[1]*Applied and Environmental Geophysics Group, University of Lausanne, CH-1015 Lausanne, Switzerland. E-mail: rsidler@gmail.com*
[2]*Istituto Nazionale di Oceanografia e di Geofisica Sperimentale (OGS), Borgo Grotta Gigante 42c, I-34010 Sgonico, Trieste, Italy*

SUMMARY

We present a novel approach for the comprehensive, flexible and accurate simulation of poroelastic wave propagation in 3-D cylindrical coordinates. An important application of this method is the realistic modelling of complex seismic wave phenomena in fluid-filled boreholes, which represents a major, as of yet largely unresolved, problem in exploration geophysics. To this end, we consider a numerical mesh consisting of three concentric domains representing the borehole fluid in the centre followed by the mudcake and/or casing, and the surrounding porous formation. The spatial discretization is based on a Chebyshev expansion in the radial direction and Fourier expansions in the vertical and azimuthal directions as well as a Runge–Kutta integration scheme for the time evolution. Trigonometric interpolation and a domain decomposition method based on the method of characteristics are used to match the boundary conditions at the fluid/porous-solid and porous-solid/porous-solid interfaces as well as to reduce the number of gridpoints in the innermost domain for computational efficiency. We apply this novel modelling approach to the particularly challenging scenario of near-surface borehole environments. To this end, we compare 3-D heterogeneous and corresponding rotationally invariant simulations, assess the sensitivity of Stoneley waves to formation permeability in the presence of a casing and evaluate the effects of an excavation damage zone behind a casing on sonic log recordings. Our results indicate that only first arrival times of fast modes are reasonably well described by rotationally invariant approximations of 3-D heterogenous media. We also find that Stoneley waves are indeed remarkably sensitive to the average permeability behind a perforated PVC casing, and that the presence of an excavation damage zone behind a casing tends to dominate the overall signature of recorded seismograms.

Key words: Numerical solutions; Interface waves; Seismic attenuation; Computational seismology; Wave scattering and diffraction; Wave propagation.

1 INTRODUCTION

Biot's (1962) seminal work demonstrates that pressure re-equilibration associated with a seismic wave passing through a fluid-saturated porous medium provides a direct link between seismic attenuation and permeability. To date, the most tangible application of this theoretical framework is the inversion of Stoneley waves recorded along fluid-filled boreholes for permeability (e.g. Cheng *et al.* 1987; Winkler *et al.* 1989). Stoneley waves are special types of surface waves. When travelling along fluid-filled boreholes they are also referred to as tube waves. Stoneley-wave inversion has reached some degree of maturity in hydrocarbon exploration and is now

considered a viable tool for improving permeability models of oil and gas reservoirs (e.g. Tang & Cheng 1996; Qobi *et al.* 2001; Cui *et al.* 2003; Parra *et al.* 2006; Ávila-Carrera *et al.* 2011). Although recent work by Baron & Holliger (2011) demonstrated that the *P*-wave velocity dispersion inferred from sonic logs can be used to constrain the permeability of unconsolidated aquifers, the hydraulic interpretation of sonic log data from shallow boreholes in unconsolidated sediments lags far behind that of its deeper counterparts. The primary reasons for this are likely to be related to the strong heterogeneity, high compressibility and low shear strength, screened or unscreened PVC casings, and extensive excavation damage zones, which are typical of shallow borehole environments and which cannot be assessed by the widely used analytical or reflectivity-type models. Moreover, the commonly used quasi-static or rigid frame approximations, which are based on the assumption that the

---

*Now at: Department of Earth Sciences, Simon Fraser University, 8888 University Drive, Burnaby BC V5A1S6, Canada.

stiffness of the solid frame is much larger than that of the pore fluid and which consider wave propagation in the pore fluid separately from propagation in the porous frame, are likely to be invalid in unconsolidated sediments.

Seismic wave propagation in near-surface borehole environments is therefore not only extremely complex, but also largely unexplored and correspondingly poorly understood. An effective way to address this problem is through realistic numerical simulations. To our knowledge, very few corresponding efforts have been undertaken so far. Clark (1956) presented the analytical solution for torsional wave modes in hollow cylindrical rods. Based on these solutions White & Zechman (1968) calculated the response of an acoustic logging tool to flexural wave modes. Rosenbaum (1974) used a quasi-static approximation of Biot's (1956) theory of wave propagation in porous media to calculate seismograms for sonic logging experiments. Tsang & Rader (1979) used numerical methods to calculate seismograms for borehole experiments in elastic media. Norris (1989) introduced a correction term to the quasi-static solution to account for the frame compressibility of the porous medium. Guan *et al.* (2009) presented a finite difference modelling code for seismic wave propagation in rotationally invariant poroelastic media. Karpfinger *et al.* (2010) proposed a spectral method to calculate wave propagation in boreholes with radially nested homogeneous poroelastic cylindrical layers and Käser *et al.* (2010) used a discontinuous Galerkin method to simulate elastic wave propagation in boreholes with arbitrary model geometry and heterogeneity.

Here, we present a generic numerical method to simulate wave propagation in heterogeneous porous media in 3-D cylindrical coordinates. The use of a poroelastic approach is essential given that a key objective of borehole seismic experiments is the estimation of the governing hydraulic characteristics of the surrounding geological formations (e.g. Norris 1989; Klimentos & McCann 1990; Tang & Cheng 2004; Lin *et al.* 2009). The proposed method is based on a pseudospectral domain decomposition approach using multiple domains that are connected by an approach based on the method of characteristics (Carcione *et al.* 2002). We use Chebyshev differentiation along the radial direction and Fourier operators along the

vertical and azimuthal directions. The viability and accuracy of the proposed method has been tested and verified in 2-D polar coordinates through comparisons with analytical solutions as well as with the results of a corresponding and independently benchmarked solution for 2-D Cartesian coordinates (Sidler *et al.* 2013). In addition to the simulation of borehole seismic experiments *sensu strictu*, potential applications of this approach can, for example, be found in the planning and/or evaluation of laboratory-scale experiments, the development of borehole seismic tools or the optimized design of borehole casings.

2 NUMERICAL SOLUTION

Pseudospectral methods are efficient and highly accurate techniques for the modelling of complex wave propagation phenomena (e.g., Kessler & Kosloff 1991; Fornberg 1996; Carcione 2007; Sidler *et al.* 2010; Liu *et al.* 2011). They can be viewed as the limit of finite differences with infinite order of accuracy, as the spatial derivatives are calculated in the wavenumber domain using a forward and backward discrete Fourier transform (Fornberg 1988; Boyd 2001). When physical boundary conditions are to be satisfied, the Fourier method is replaced by the Chebyshev method, which is not periodic and allows for an explicit boundary treatment by decomposing the wavefields using characteristic variables and updating the modelling domain with appropriate boundary conditions (Carcione *et al.* 2002). For this reason, we use the Chebyshev differential operator along the radial direction and Fourier operators along the other directions. We use a fourth-order Runge–Kutta method to solve the stress–strain relations and the equations of motion, where the same time step is used for all domains.

We consider a 3-D cylindrical coordinate system and use independent computational domains for the individual components of the borehole model (Fig. 1). The innermost domain represents the fluid and is followed by two or more outer domains that represent the casing and the surrounding porous formation. For the fluid filling the borehole, we use an acoustic domain supporting only one compressional wave mode. For the casing and the surrounding formation we use two poroelastic domains that support a slow and a fast
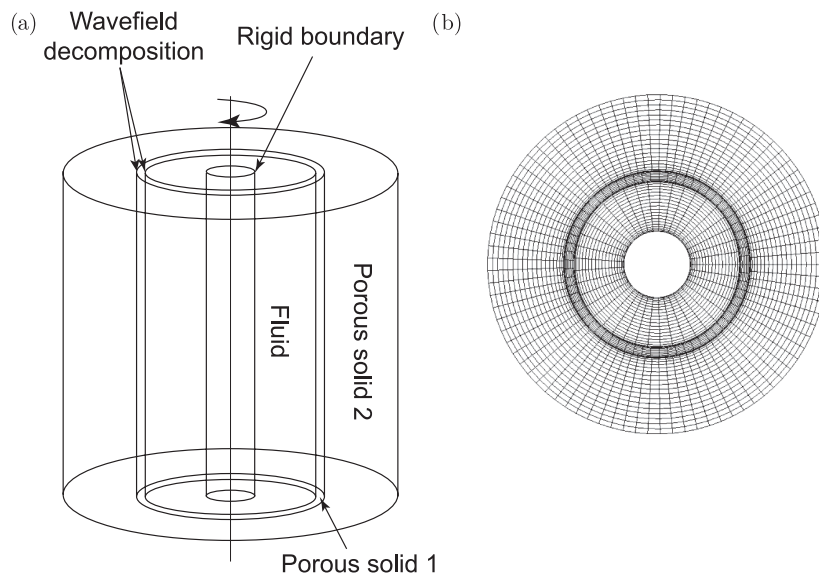

Figure 1. Basic model setup for the proposed modelling approach consisting of three computational domains. The innermost domain is acoustic, while the outer two domains are poroelastic. The wavefield is decomposed at the interfaces of the domains and the adjacent domains are updated according to the governing boundary conditions. (a) The whole modelling domain and (b) grid node locations on a section in the $(r - \theta)$ plane are shown. To represent the borehole logging tool, the innermost boundary conditions correspond to those of a rigid surface. The centre of the acoustic domain is void.

compressional wave mode as well as a shear wave mode. An equivalent porous medium is used for the characterization of screened and non-screened PVC casings. The non-screened casing is characterized by low porosity and permeability, which in turn results in a quasi-elastic behaviour. The independent domains are combined by decomposing the wavefields based on the method of characteristics into incoming and outgoing wave modes at the interfaces between the domains and by modifying these modes on the basis of the governing boundary conditions. The boundary conditions at fluid/poroelastic interfaces can be of the open-pore, closed-pore or mixed-pore type (Deresiewicz & Skalak 1963).

In the following, we present the equations governing wave propagation in porous media. A list of the used symbols is given in Appendix A. The constitutive equations for a poroelastic medium are (Carcione 2007)

$$\boldsymbol{\tau} = [(E_\mathrm{m} - 2\mu + M\alpha^2)\nabla \cdot \mathbf{u} + \alpha M\nabla \cdot \mathbf{u}_\mathrm{f}]\mathbf{I} + \mu[\nabla\mathbf{u} + \nabla\mathbf{u}^\top], \quad (1)$$

$$-p = \alpha M\nabla \cdot \mathbf{u} + M\nabla \cdot \mathbf{u}_\mathrm{f}, \quad (2)$$

where $\boldsymbol{\tau}$ is the stress tensor, p the pore fluid pressure, $\mathbf{I}$ denotes the identity matrix and μ is the shear modulus of the bulk material, considered to be equal to the shear modulus of the dry matrix. The operators ∇ and $\nabla \cdot$ denote the gradient and divergence, respectively. The relative fluid displacement is defined as $\mathbf{u}_\mathrm{f} = \phi(\mathbf{U} - \mathbf{u})$ with $\mathbf{U}$ denoting the fluid displacement and $\mathbf{u}$ the solid displacement vector. The dry rock fast P-wave modulus E_m is defined as

$$E_\mathrm{m} = K_\mathrm{m} + \frac{4}{3}\mu, \quad (3)$$

with K_m being the frame bulk modulus. The poroelastic incompressibility M, which is a fluid storage coefficient since it quantifies the amount of fluid stored in a sample of constant size when the fluid pressure is increased, is defined as

$$M = \left(\frac{\alpha - \phi}{K_\mathrm{s}} + \frac{\phi}{K_\mathrm{f}}\right)^{-1}, \quad (4)$$

with ϕ, K_s and K_f denoting the porosity, the grain bulk modulus and the pore fluid bulk modulus, respectively. The coefficient α is known as the effective stress coefficient of the bulk material and is given by

$$\alpha = 1 - \frac{K_\mathrm{m}}{K_\mathrm{s}}. \quad (5)$$

In the following equations, we use the solid and relative fluid particle velocity vectors $\mathbf{v} = \dot{\mathbf{u}}$ and $\mathbf{q} = \dot{\mathbf{u}}_\mathrm{f}$ instead of the displacement vectors, and assume that the bulk density is given by $\rho = (1 - \phi)\rho_\mathrm{s} + \phi\rho_\mathrm{f}$ with the grain density ρ_s and the pore fluid density ρ_f.

The Biot–Euler equations for a poroelastic material are

$$\tau_{rr,r} + \frac{1}{r}\tau_{r\theta,\theta} + \tau_{rz,z} + \frac{\tau_{rr} - \tau_{\theta\theta}}{r} = \rho v_{r,t} + \rho_\mathrm{f} q_{r,t}, \quad (6)$$

$$\tau_{r\theta,r} + \frac{1}{r}\tau_{\theta\theta,\theta} + \tau_{z\theta,z} = \rho v_{\theta,t} + \rho_\mathrm{f} q_{\theta,t}, \quad (7)$$

$$\tau_{rz,r} + \frac{1}{r}\tau_{\theta z,\theta} + \tau_{zz,z} + \frac{\tau_{rz}}{r} = \rho v_{z,t} + \rho_\mathrm{f} q_{z,t}, \quad (8)$$

where the subscripts ',r', ',θ' and ',z' denote the derivative in radial, azimutal and vertical directions of the specific scalar field, respectively. Similarly, the time derivative is indicated by adding the subscripts ',t'. The correspondingly subscripted scalar fields of v, q and τ are the components in r, θ and z directions of the solid and fluid vector fields and the stress tensor, respectively.

The Darcy–Euler equations are given by

$$-p_{,r} = \rho_\mathrm{f} v_{r,t} + \frac{\mathcal{T}\rho_\mathrm{f}}{\phi}q_{r,t} + \frac{\eta}{\kappa}q_r, \quad (9)$$

$$-\frac{1}{r}p_{,\theta} = \rho_\mathrm{f} v_{\theta,t} + \frac{\mathcal{T}\rho_\mathrm{f}}{\phi}q_{\theta,t} + \frac{\eta}{\kappa}q_\theta, \quad (10)$$

$$-p_{,z} = \rho_\mathrm{f} v_{z,t} + \frac{\mathcal{T}\rho_\mathrm{f}}{\phi}q_{z,t} + \frac{\eta}{\kappa}q_z, \quad (11)$$

where $\mathcal{T}$ is the tortuosity describing the 'twisting' of the actual flow path compared to a corresponding straight line. The viscosity η and the permeability κ characterize the flow resistance η/κ of the pore fluid and are not meant to contribute independently to wave propagation in Biot's theory. Eqs (6)–(11) can be recast as

$$v_{r,t} = \gamma_{11}\left(\tau_{rr,r} + \frac{\tau_{r\theta,\theta}}{r} + \frac{\tau_{rr} - \tau_{\theta\theta}}{r} + \tau_{rz,z}\right) + \gamma_{12}\left(p_{,r} + \frac{\eta}{\kappa}q_r\right), \quad (12)$$

$$q_{r,t} = -\gamma_{12}\left(\tau_{rr,r} + \frac{\tau_{r\theta,\theta}}{r} + \frac{\tau_{rr} - \tau_{\theta\theta}}{r} + \tau_{rz,z}\right) + \gamma_{22}\left(p_{,r} + \frac{\eta}{\kappa}q_r\right), \quad (13)$$

$$v_{\theta,t} = \gamma_{11}\left(\frac{\tau_{\theta\theta,\theta}}{r} + \tau_{r\theta,r} + \tau_{z\theta,z}\right) + \gamma_{12}\left(\frac{p_{,\theta}}{r} + \frac{\eta}{\kappa}q_\theta\right), \quad (14)$$

$$q_{\theta,t} = -\gamma_{12}\left(\frac{\tau_{\theta\theta,\theta}}{r} + \tau_{r\theta,r} + \tau_{z\theta,z}\right) + \gamma_{22}\left(\frac{p_{,\theta}}{r} + \frac{\eta}{\kappa}q_\theta\right), \quad (15)$$

$$v_{z,t} = \gamma_{11}\left(\tau_{rz,r} + \tau_{zz,z} + \frac{1}{r}(\tau_{z\theta,\theta} + \tau_{rz})\right) + \gamma_{12}\left(p_{,z} + \frac{\eta}{\kappa}q_z\right), \quad (16)$$

$$q_{z,t} = -\gamma_{12}\left(\tau_{rz,r} + \tau_{zz,z} + \frac{1}{r}(\tau_{z\theta,\theta} + \tau_{rz})\right) + \gamma_{22}\left(p_{,z} + \frac{\eta}{\kappa}q_z\right), \quad (17)$$

with

$$\gamma_{11} = \frac{\mathcal{T}}{\rho\mathcal{T} - \phi\rho_\mathrm{f}}, \quad \gamma_{12} = \frac{\phi}{\rho\mathcal{T} - \phi\rho_\mathrm{f}} \quad \text{and} \quad \gamma_{22} = \frac{\rho}{\rho_\mathrm{f}}\frac{\phi}{\phi\rho_\mathrm{f} - \rho\mathcal{T}}. \quad (18)$$

The stress–strain relations can be written as

$$\tau_{rr,t} = (E_\mathrm{m} - 2\mu + M\alpha^2)\nabla \cdot v + \alpha M\nabla \cdot q + 2\mu v_{r,r}, \quad (19)$$

$$\tau_{\theta\theta,t} = (E_\mathrm{m} - 2\mu + M\alpha^2)\nabla \cdot v + \alpha M\nabla \cdot q + \frac{2\mu}{r}(v_{\theta,\theta} + v_r), \quad (20)$$

$$\tau_{zz,t} = (E_\mathrm{m} - 2\mu + M\alpha^2)\nabla \cdot v + \alpha M\nabla \cdot q + 2\mu v_{z,z}, \quad (21)$$

$$\tau_{r\theta,t} = \mu\left(\frac{1}{r}(v_{r,\theta} - v_\theta) + v_{\theta,r}\right), \quad (22)$$

$$\tau_{rz,t} = \mu(v_{r,z} + v_{z,r}), \quad (23)$$

$$\tau_{z\theta,t} = \mu\left(\frac{v_{z,\theta}}{r} + v_{\theta,z}\right), \quad (24)$$

$$p_{,t} = -M[\nabla \cdot q + \alpha(\nabla \cdot v)], \quad (25)$$

where

$$\nabla \cdot v = \frac{1}{r}(r \cdot v_r)_{,r} + \frac{1}{r}v_{\theta,\theta} + v_{z,z}, \quad (26)$$

and

$$\nabla \cdot q = \frac{1}{r}(r \cdot q_r)_{,r} + \frac{1}{r}q_{\theta,\theta} + q_{z,z}, \quad (27)$$

with μ being the shear modulus.

The equations of motion for the acoustic domain in the centre with a fluid of density ρ_a and bulk modulus K_a are given by the stress–strain relation

$$\dot{p}_a = K_a \left[w_{r,r} + \frac{1}{r}(w_{\theta,\theta} + w_r) + w_{z,z} \right], \tag{28}$$

and Euler's equations

$$p_{a,r} = \rho_a \dot{w}_r, \quad \frac{1}{r} p_{a,\theta} = \rho_a \dot{w}_\theta \quad \text{and} \quad p_{a,z} = \rho_a \dot{w}_z, \tag{29}$$

where p_a and w denote the fluid pressure and particle velocity, respectively.

2.1 Rotational symmetry around the borehole axis

The 3-D cylindrical solution is computationally expensive and for many practically relevant problems a realistic approximation is to assume symmetry with regard to the vertical axis. An elegant method to compute the cylindrically symmetric wavefield was shown by Randall *et al.* (1991) and by Randall (1991). When applying the Fourier transform in the azimuthal direction of the 3-D solution, the derivative in azimuthal direction becomes a multiplication with the azimuthal wavenumber k_θ. By explicitly choosing the azimuthal dependencies in the frequency–wavenumber domain for v_r, q_r, v_z, q_z, τ_{rr}, $\tau_{\theta\theta}$, τ_{zz}, τ_{rz} to be proportional to $\cos(m\theta)$ and for v_θ, q_θ, $\tau_{r\theta}$, $\tau_{\theta z}$, p to be proportional to $\sin(m\theta)$ the source characteristics are reduced to a symmetrical distribution around the z-axis with an azimuthal shape factor m. In the time domain, the derivatives in azimuthal directions then simplify to a multiplication with this shape factor (Carcione & Poletto 2008; Carcione *et al.* 2008).

Some important aspects of the 3-D nature of the wavefield, such as the source radiation and spreading characteristics, are retained and the computational cost is dramatically reduced. At the same time, the heterogeneity of the medium also reduces to two dimensions, which leads to a significant reduction in memory consumption.

The shape factor m defines the symmetry of the source. A monopole source corresponds to $m = 0$, a dipole source to $m = 1$, a quadrupole source to $m = 2$, and so on.

For the assumption of azimuthal invariance, the equations of motion (eqs 12–17) reduce to

$$v_{r,t} = \gamma_{11} \left(\tau_{rr,r} + \frac{m}{r}\tau_{r\theta} + \frac{\tau_{rr} - \tau_{\theta\theta}}{r} + \tau_{rz,z} \right) + \gamma_{12} \left(p_{,r} + \frac{\eta}{\kappa} q_r \right), \tag{30}$$

$$q_{r,t} = -\gamma_{12} \left(\tau_{rr,r} + \frac{m}{r}\tau_{r\theta} + \frac{\tau_{rr} - \tau_{\theta\theta}}{r} + \tau_{rz,z} \right) + \gamma_{22} \left(p_{,r} + \frac{\eta}{\kappa} q_r \right), \tag{31}$$

$$v_{\theta,t} = \gamma_{11} \left(\tau_{r\theta,r} - \frac{m}{r}\tau_{\theta\theta} + \tau_{z\theta,z} \right) + \gamma_{12} \left(\frac{m}{r}p + \frac{\eta}{\kappa} q_\theta \right), \tag{32}$$

$$q_{\theta,t} = -\gamma_{12} \left(\tau_{r\theta,r} - \frac{m}{r}\tau_{\theta\theta} + \tau_{z\theta,z} \right) + \gamma_{22} \left(\frac{m}{r}p + \frac{\eta}{\kappa} q_\theta \right), \tag{33}$$

$$v_{z,t} = \gamma_{11} \left(\tau_{rz,r} + \tau_{zz,z} + \frac{m}{r}\tau_{z\theta} + \frac{\tau_{rz}}{r} \right) + \gamma_{12} \left(p_{,z} + \frac{\eta}{\kappa} q_z \right), \tag{34}$$

$$q_{z,t} = -\gamma_{12} \left(\tau_{rz,r} + \tau_{zz,z} + \frac{m}{r}\tau_{z\theta} + \frac{\tau_{rz}}{r} \right) + \gamma_{22} \left(p_{,z} + \frac{\eta}{\kappa} q_z \right), \tag{35}$$

and the stress–strain relations (eqs 19–25) to

$$\tau_{rr,t} = (E_m - 2\mu + M\alpha^2)\nabla \cdot v + \alpha M\nabla \cdot q + 2\mu v_{r,r}, \tag{36}$$

$$\tau_{\theta\theta,t} = (E_m - 2\mu + M\alpha^2)\nabla \cdot v + \alpha M\nabla \cdot q + \frac{2\mu}{r}(m \cdot v_\theta + v_r), \tag{37}$$

$$\tau_{zz,t} = (E_m - 2\mu + M\alpha^2)\nabla \cdot v + \alpha M\nabla \cdot q + 2\mu v_{z,z}, \tag{38}$$

$$\tau_{r\theta,t} = \mu \left(v_{\theta,r} - \frac{m}{r}v_r - \frac{1}{r}v_\theta \right), \tag{39}$$

$$\tau_{rz,t} = \mu(v_{r,z} + v_{z,r}), \tag{40}$$

$$\tau_{z\theta,t} = \mu \left(v_{\theta,z} - \frac{m}{r}v_z \right), \tag{41}$$

$$p_{,t} = -M[\nabla \cdot q + \alpha(\nabla \cdot v)]. \tag{42}$$

2.2 Boundary conditions

In the following, we describe which interfaces need special treatment and how we implement the corresponding boundary conditions. We use the approach of Gottlieb *et al.* (1982) to simulate the propagation of seismic waves within the individual domains independently of each other and to connect these domains with each other. We decompose the outgoing wavefield at the boundaries using characteristic variables and update the field variables as explained later. For computational efficiency, we use different numbers of gridpoints in the azimuthal direction for individual domains in the 3-D simulations. We therefore use a trigonometric interpolation to obtain the field variables at the azimuthal locations of opposite grid nodes (Atkinson 1989). As the grid nodes are equally spaced in the azimuthal direction, we can use a discrete Fourier transform to perform this interpolation. The same kind of boundary treatment in Cartesian and polar coordinates was used by Carcione (1991), Kessler & Kosloff (1991) and Tessmer *et al.* (1992) for elastic media and by Sidler *et al.* (2010, 2013) for poroelastic media. The derivation of the characteristic vector for wave propagation in radial direction for a poroelastic medium in cylindrical coordinates is shown in Appendix B. The solution of the linear system with the appropriate characteristics and the boundary conditions for a specific interface reveals how to update the field variables at this boundary.

The rigid inner boundary of the acoustic domain and therefore the innermost boundary of the model space can be seen as corresponding to the outer shell of a borehole tool. It is difficult to comprehensively model a borehole tool as it consists of a large number of parts with complex shapes. As a first approximation, the tool can be considered as a metal cylinder with an effective bulk modulus. As the bulk modulus of metal is considerably higher than that of the pore fluid, it is reasonable to assume rigid boundary conditions at the interface and to neglect wave propagation inside the tool (Norris 1990; Tang & Cheng 1993; Carcione & Poletto 2008).

Ignoring the wave propagation inside the borehole tool is a shortcoming of the method. On the other hand, it can be argued that the suppression of wave propagation along and inside the tool is a vital concern for tool developers as, due to the high bulk modulus and the prevailing geometry, waves propagating in the tool would arrive first at the receiver thus obscuring the actual formation signal. Norris' (1990) example for changes in tube wave speed due to the presence of a borehole tool may give an impression of the order-of-magnitude of the effect: A 6-cm-diameter tool is placed

in a 10-cm-diameter borehole which changes the tube wave speed from 1292 m s^{-1} without a tool to 1201 m s^{-1} when assuming a steel tool and to 1207 m s^{-1} when rigid boundary conditions are used. The shear very presence of a tool in the simulation and the diameter of the tool thus seem to have a much stronger influence on the resulting seismograms than the detailed properties of the borehole tool. Appendix B1 outlines the corresponding boundary conditions and explains how to update the field variables at the innermost grid-point of the fluid domain when using the wavefield decomposition approach considered in this study.

The outer boundary of the acoustic domain is connected to the first porous domain. Here we use the boundary conditions of Deresiewicz & Skalak (1963) and employ the surface flow impedance to account for the non-uniqueness of the equations when applying the energy conservation law. The physical meaning of the surface flow impedance is the interconnection of the pore space of two adjacent media at an interface. The pore space can be fully or partially connected or entirely disconnected and the corresponding boundary conditions are referred to as open-, mixed- or closed-pore boundary conditions, respectively. We have implemented the entire range of boundary conditions for the interface between the acoustic and the first poroelastic domain as we think it has an important physical meaning describing the condition of the borehole wall when the pores are clogged by deposits such as, for example, drilling mud (Appendix B2). For the boundary between the first and the second porous domain, we have restricted the implementation to open-pore boundary conditions assuming a connected pore space (Appendix B3). For the outer boundary of the second porous solid, we use non-reflecting boundary conditions. That is, we keep the outgoing characteristics and set the inward propagating wave modes to zero (Appendix B4). This sort of boundary conditions absorb the normally incident part of the impinging waves. Due to the geometry and the fact that we place the sources for the sonic experiments mostly close to the centre of the modelling domain, these boundary conditions prevent non-physical reflections from the edges of the modelling domain even more effectively than in Cartesian coordinates. To further enhance the absorbing properties, we also add a diffusive strip to the outermost boundary (Carcione & Kosloff 2013).

3 SIMULATIONS

3.1 Comparison of seismic wave propagation in 3-D heterogeneous media and corresponding rotationally invariant media

Using the methods described above, we compare wave propagation in 3-D heterogeneous media to wave propagation in corresponding cylindrically invariant media. The latter approach is computationally much more efficient, but the implications of assuming rotational symmetry for 3-D heterogeneous environments are not clear. Both approaches have 3-D spreading characteristics and hence can be easily compared. The goal is to explore to what extent a simplified rotationally invariant model can be used for simulations of seismic wave propagation in heterogeneous formations.

We create a 3-D heterogeneous poroelastic model in Cartesian coordinates and use an algorithm to search for the closest corresponding grid node to populate the parametrization in cylindrical coordinates. We start with a heterogeneous porosity distribution generated with the spectral method, which provides a second-order stationary realization of a random variable with a given mean value and auto-
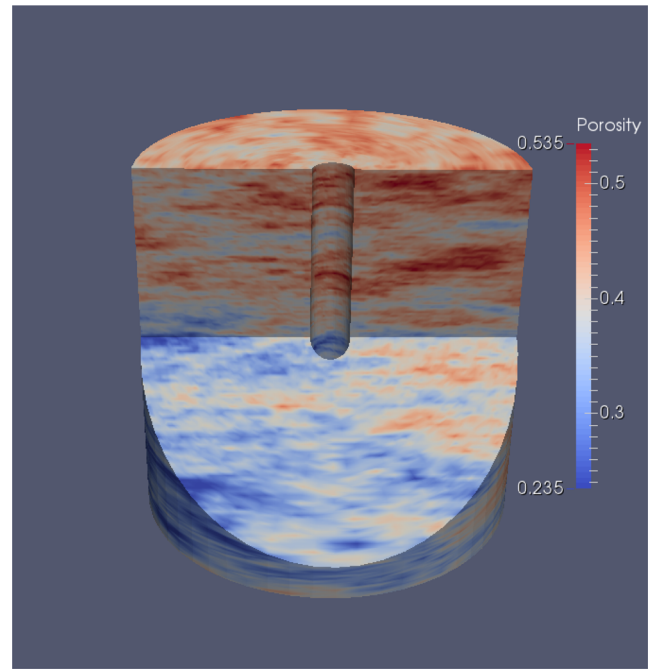

Figure 2. 3-D heterogeneous porosity model characterized by a von Kármán auto-covariance function with $\nu = 0.2$ and a ratio between radial and vertical correlation lengths a_r/a_z of 6. The values are normally distributed around a mean of 38 per cent and have a standard deviation of 5 per cent. See also Appendix C.

Table 1. Material properties of unconsolidated marine sand (Jackson & Richardson 2007).

Grain	K_s	32 GPa
	μ_s	44 GPa
	ρ_s	2690 kg m^{-3}
Matrix	K_m	1.36 GPa
	μ	1.86 GPa
	ϕ	0.38
	κ	28.3 D
	$\mathcal{T}$	1.8
Fluid	ρ_f	1000 kg m^{-3}
	η	0.00105 Pa s
	K_f	2.25 GPa

covariance function (Appendix C1). An illustration of the resulting porosity model is shown in Fig. 2. We have chosen a realization based on a von Kármán auto-covariance function with a mean of 38 per cent, a standard deviation of 5 per cent and a strong spatial variability characterized by a ν-value of 0.2. ν-values close to zero emulate the ubiquitous and seemingly universal flicker noise character of sonic log data (e.g. Holliger & Goff 2003). The porosity is discretized in Cartesian coordinates in a mesh with $300 \times 300 \times 300$ nodes. The cylindrical domain, which has $55 \times 55 \times 151$ grid nodes in the r, θ and z directions, respectively, is centred in this mesh with the values of the closest corresponding node assigned accordingly.

Based on this porosity distribution, we estimate the other poroelastic model parameters using empirical relationships. The relationships used in Appendix C2 were computed with the solid grain properties shown in Table 1.

To obtain the input models for the rotationally invariant simulations that are then compared to the corresponding 3-D simulations, we cut six vertical slices through the 3-D porosity model, which
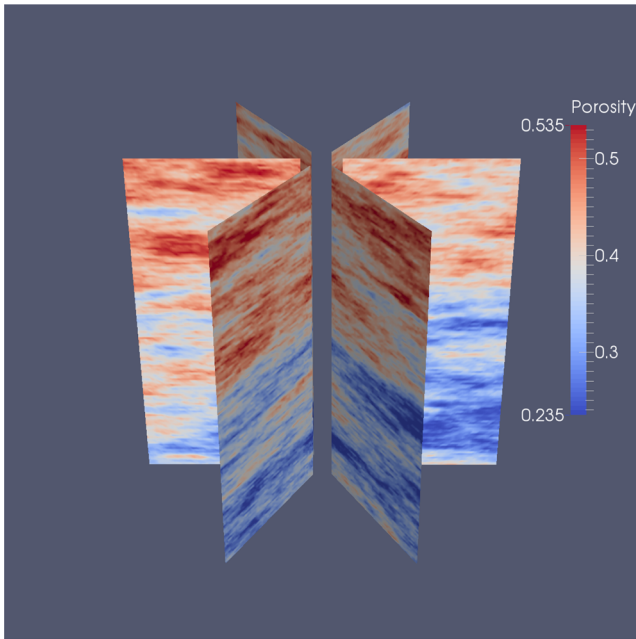
Figure 3. Six 2-D porosity models for the rotationally invariant simulations obtained by vertically cutting through the 3-D model shown in Fig. 2.

Table 2. Poroelastic material properties of a screened PVC casing (Barrash *et al.* 2006; Bakulin *et al.* 2008).

Grain	K_s	4.049 GPa
	μ_s	1.248 GPa
	ρ_s	1400 kg m^{-3}
Matrix	K_m	3.482 GPa
	μ	1.211 GPa
	ϕ	0.04 / 0.10
	κ	1900 D (1 D $= 9.86233 \cdot 10^{-13}$ m^2)
	$\mathcal{T}$	1.5
Fluid	ρ_f	1000 kg m^{-3}
	η	0.001 Pa s
	K_f	2.25 GPa

are evenly distributed along the azimuthal direction. The resulting slices are shown in Fig. 3.

The innermost radius of the acoustic domain is 0.019 m, which corresponds to the rigid surface of the borehole tool. The outer radius of the acoustic domain corresponding to the borehole wall is 0.075 m. The bulk modulus and density of the acoustic domain have the same properties as the fluid filling the pore space in the surrounding formation. The first porous domain has the properties of a screened PVC casing shown in Table 2 and the second porous domain corresponds to unconsolidated sand characterized in Table 1. The number of gridpoints in the z-direction is 151 and 13/13 for the acoustic, 7/25 for the first and 55/55 for the second porous domain are used along the radial/angular directions. These simulations where run for 50 000 time steps of 2.5×10^{-8} s. The source is a monopole or ring source with the time history of a Ricker wavelet centred at 9 kHz applied at the inner boundary of the fluid domain. For the rotationally invariant simulations the same grid sizes are used for the directions different from the angular direction.

Fig. 4 shows the corresponding seismograms recorded at the borehole wall for a vertical distance of 0.35, 0.55 and 0.80 m from the source. The red curve shows the solution for the 3-D hetero-
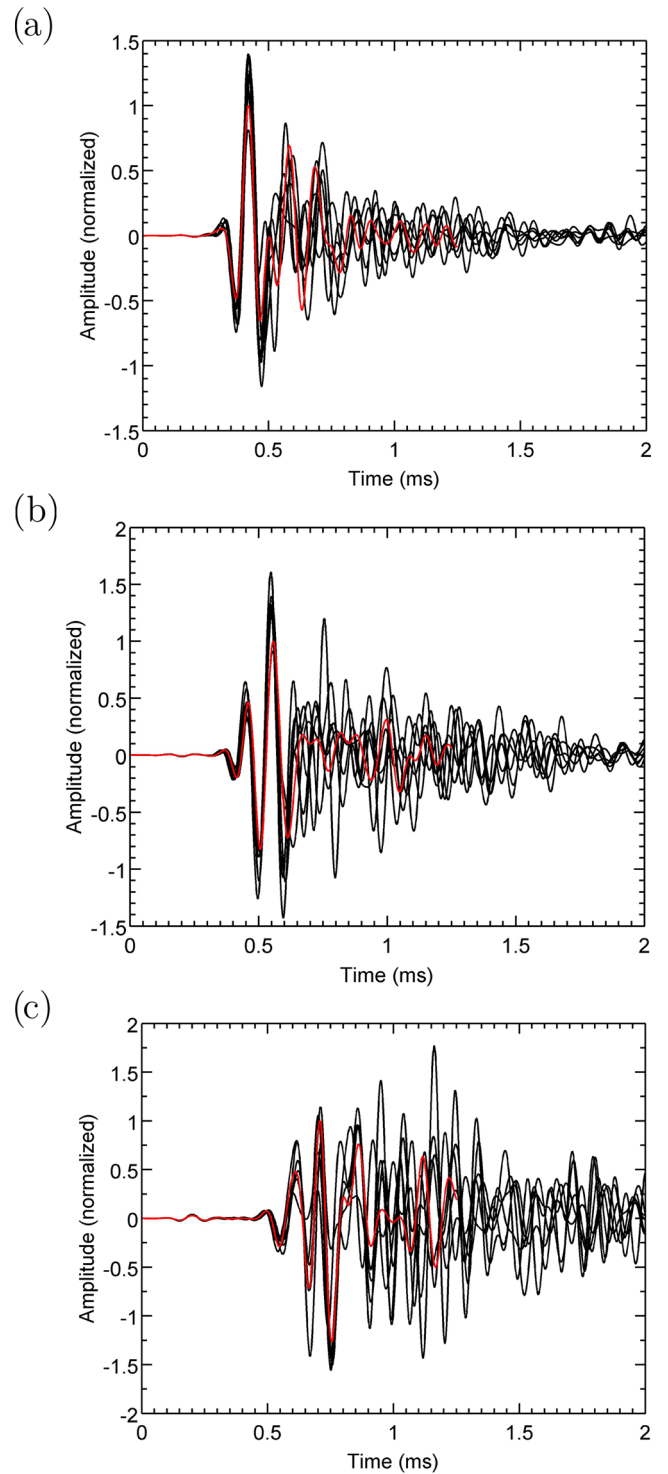

Figure 4. Seismograms recorded at the borehole wall at a vertical distance of (a) 0.35 m, (b) 0.55 m and (c) 0.80 m from the source for the model based on the porosity distribution shown in Fig. 2. The red line shows the solution for the 3-D heterogeneous model (Fig. 2) and the black lines correspond to the solutions for the six rotationally invariant heterogeneous models based on vertical cuts through the 3-D model (Fig. 3). The seismograms are normalized with respect to the maximum amplitude of the 3-D solution.

geneous cylindrical solution and the black lines correspond to the solutions for the six rotationally invariant solutions shown in Fig. 3. The seismograms are normalized to the maximum amplitude of the 3-D solution. It can be seen that phases and amplitudes for early

arrivals are well approximated by the rotationally invariant solutions. This is also true for larger source–receiver offsets where the absolute amplitudes are lower and the effect of scattering becomes stronger. For later arrivals, the discrepancies between the solutions for the 3-D heterogeneous model and for the rotationally invariant models are systematically high and increase with increasing offset. Again, the amplitudes are more strongly affected than the phases. This can be explained by the fact that the shear wave is more strongly affected by the heterogeneities than the fast compressional wave due to the slower velocity and the correspondingly larger heterogeneities with respect to the dominant wavelength. Indeed, the Stoneley wave can no longer be detected in the rotationally symmetric solutions, whereas this wave mode can be clearly identified in the 3-D heterogeneous case.

Scattering is strongly dependent on the detailed character of the heterogeneity of the medium in which the wave propagates. We have therefore repeated the above-mentioned experiment for heterogeneous media with different porosity distributions, correlation lengths and standard deviations. We have obtained consistent results and came to the same conclusions as for the example discussed above, which are based on a rather strongly heterogeneous medium. The results for a more moderate heterogeneity as characterized by a standard deviation of 2 per cent for the underlying porosity distribution are shown in Fig. 5.

Fig. 6 shows snapshots illustrating the effects of heterogeneity. We compare a homogeneous medium (Fig. 6a) with a comparable heterogeneous medium (Fig. 6b). The heterogeneous model is based on the porosity distribution shown in Fig. 2, and the formation properties of the homogeneous formation are given in Table 1. In the homogeneous model, the individual wave modes as well as conversions between these modes can be clearly identified. Conversely, the heterogeneous solution is largely dominated by scattered waves that cannot easily be assigned to any specific wave modes.

3.2 Sensitivity of Stoneley waves to formation permeability behind a casing

Stoneley waves are a particular form of surface waves propagating along fluid–solid interfaces. For elastic media and planar interfaces Stoneley waves are not subject to dispersion. They can, however, become dispersive in poroelastic media. In a borehole-type setup, Stoneley waves become slightly dispersive even in the elastic limit due to waveguide effects (Haldorsen *et al.* 2006). In most cases of practical importance, the poroelasticity of the surrounding formation does, however, dominate their attenuation and dispersion behaviour. This in turn allows for relating the hydraulic properties of the formation surrounding a borehole to seismic wave propagation and can be exploited for the estimation of permeability (e.g. White 1965; Rosenbaum 1974; Winkler *et al.* 1989). The effect of a casing on such permeability estimates in particular and to sonic log recordings in general is as of yet largely unknown and of particular interest for shallow boreholes, which tend to be cased to prevent the collapse of the drilled unconsolidated sediments.

To address this question, we consider models for an uncased and two-cased boreholes with one of the casings being screened and the other one not. In an additional set of simulations, we assess how formation heterogeneity may influence the recorded seismograms. For this purpose, we again use the porosity distribution shown in Fig. 3(a), albeit with a somewhat smaller standard deviation of 2 per cent. For each scenario, we then evaluate the sensitivity of the Stoneley wave to permeability.
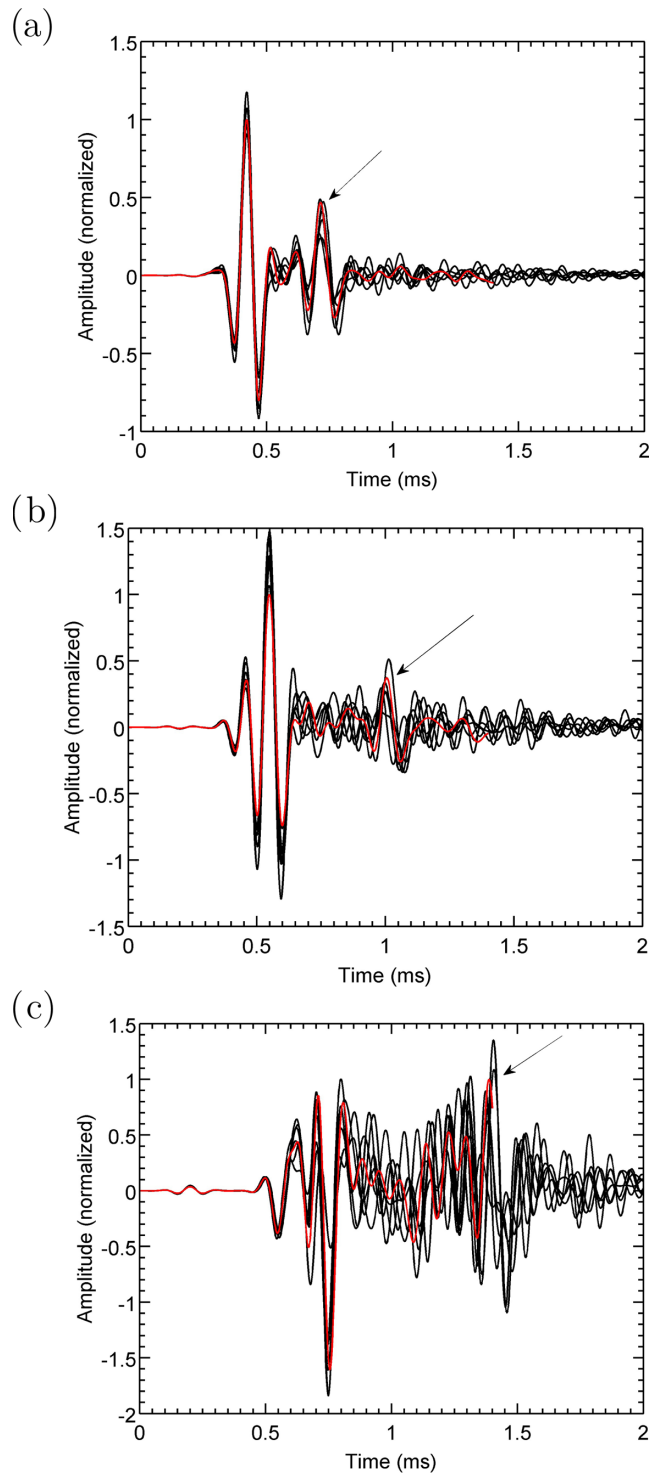

Figure 5. Same as Fig. 4, but for a model based on a porosity distribution with a standard deviation of 2 per cent. The arrow denotes the Stoneley wave.

The ease with which a fluid can flow through a porous or fractured medium depends both on the formation's permeability as well as on fluid's viscosity. This finds its expression in the fact the corresponding terms in the governing differential equations are consistently characterized by the ratio between viscosity η and the permeability κ. Setting the viscosity η to zero hence also results in a vanishing effect of the permeability κ. To test a model for its
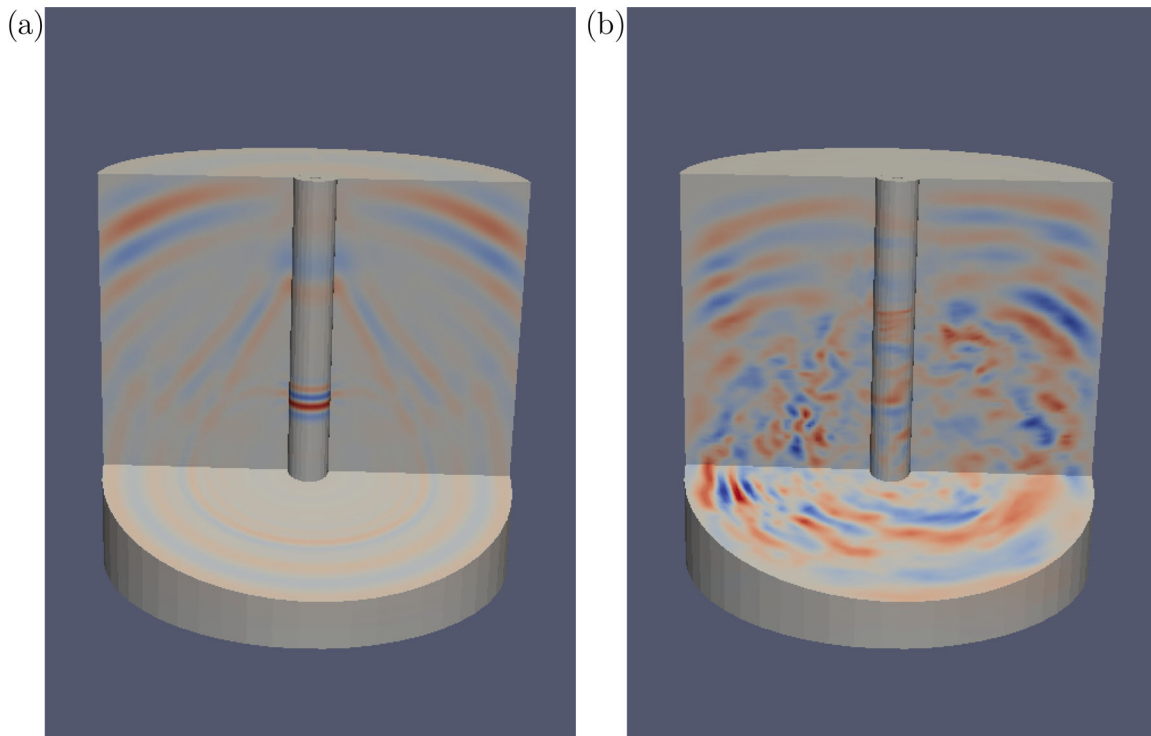
Figure 6. Snapshots of the solid pressure of the wavefield after a propagation time of 0.775 ms for (a) a homogeneous model with properties shown in Table 1 and (b) the 3-D heterogeneous model based on the porosity distribution shown in Fig. 2.

sensitivity to permeability, we therefore perform two simulations which differ only in terms of the viscosity of the pore fluid: in one simulation, we set the viscosity to that of water, while in the other one, we set the viscosity to zero. For the cased borehole models, we perform an additional simulation to characterize the effects of permeability due to the casing by considering a non-viscous pore fluid in the formation while the pore fluid of the casing is assigned the viscosity of water.

The radius of the logging tool and the borehole are considered to be 19 mm and 75 mm, respectively. We use 13, 9 and 55 gridpoints in the radial direction for the acoustic as well as the first and the second porous domain, respectively, and 351 gridpoints in the vertical direction. A receiver recording the fluid pressure is located at a vertical distance of 0.5 m from the source at the inner boundary of the casing. As the individual domains in the model are homogeneous, we use the rotationally invariant version of our algorithm in conjunction with a monopole source with the time history of a Ricker wavelet centred at 9 kHz at the inner boundary of the acoustic domain.

For the models with screened and unscreened casings, we set the properties of the inner porous domain to those of PVC to emulate a typical casing used to stabilize surficial boreholes. The thickness of the casing is assumed to be 5 mm. The material properties of PVC are adopted from Bakulin *et al.* (2008) and are shown in Table 2. There are, however, differing opinions with regard to the porosity and permeability of typical screened PVC casings. We use a porosity of 4 per cent (Bakulin *et al.* 2008) and a permeability of 1900 D (Barrash *et al.* 2006).

The seismograms corresponding to the reference model of an uncased borehole penetrating a homogeneous sandy formation (Table 1) are shown in Fig. 7. The dashed line refers to the case of a non-viscous pore fluid and the solid line to a pore fluid with the
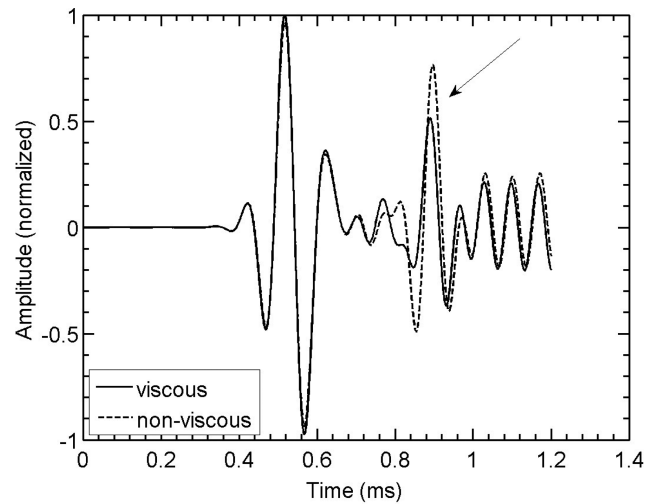

Figure 7. Sensitivity to formation permeability for an uncased borehole penetrating a homogeneous sandy formation (Table 1). Two numerical simulations are performed, one with a non-viscous pore fluid (dashed line) and one with a pore fluid that has the viscosity of water (solid line). The difference between the two seismograms characterizes the sensitivity of the data to permeability. The arrow denotes the Stoneley wave.

viscosity of water. Our results demonstrate that the Stoneley wave is very sensitive to permeability while the direct compressional wave is largely insensitive to this property.

The seismograms for a screened casing are shown in Fig. 8, where the dotted, dashed and solid lines correspond to the simulations considering no viscous dissipation, viscous dissipation only in the surrounding formation and throughout the entire model, respectively. The results indicate that the effect of the screened casing
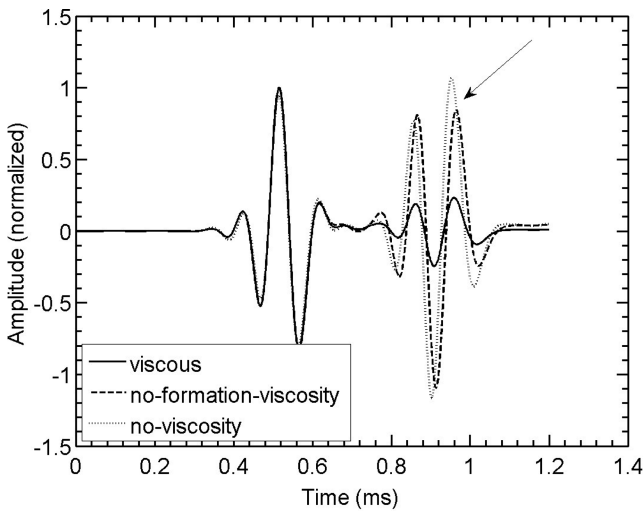
Figure 8. Same as Fig. 7, but for a borehole with a screened casing. Here, three seismograms are shown. The dotted line represents the seismogram for a non-viscous pore fluid in the casing and the formation. The dashed line corresponds to the solution with a non-viscous pore fluid in the formation and illustrates the effect of the casing. The solid line denotes the solution for a pore fluid with the viscosity of water. The arrow indicates the Stoneley wave.
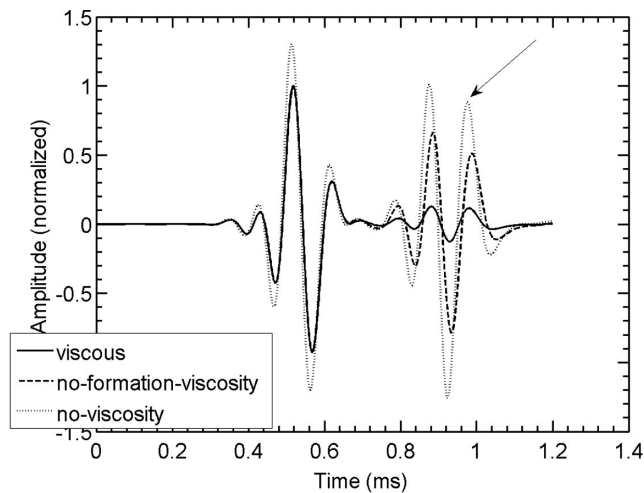

Figure 9. Same as Fig. 8, but for a borehole with a casing that is not screened. The sensitivity to pore fluid viscosity and formation permeability is strongly reduced compared to the scenarios containing a screened casing (Fig. 8) or no casing at all (Fig. 7). The arrow denotes the Stoneley wave.

is surprisingly weak. This might be due to the fact that the permeability of the casing is very high and offers correspondingly little resistance to the wave-induced fluid flow between the borehole and the surrounding formation. We have therefore repeated this numerical experiment for lower permeabilities of the casing and found that our original findings remain valid as long as the permeability of the casing is not substantially lower than that of the formation surrounding the casing.

The corresponding seismograms for a non-screened casing are shown in Fig. 9. The permeability and porosity of this non-screened casing are assumed to be of 0.01 mD and 0.005, respectively. The bulk and shear moduli of the matrix are the same as for those of the solid grain and hence the seismic behaviour of this casing is quasi-elastic. In contrast to the screened casing, the effect of an unscreened casing on the propagation of the Stoneley wave is
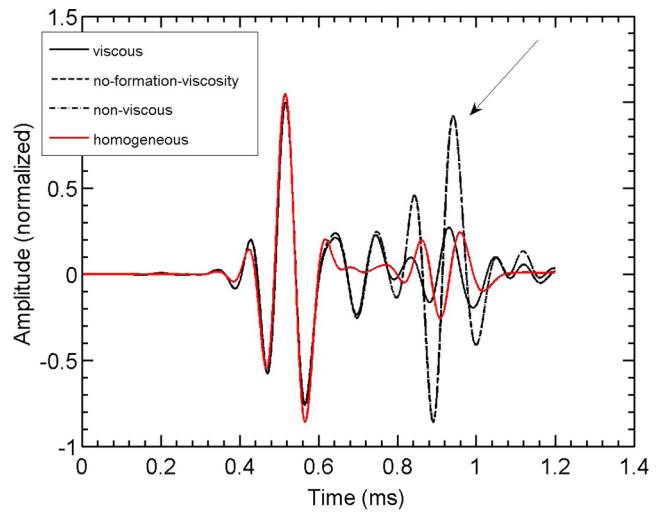

Figure 10. Same as Fig. 8, but for a heterogeneous formation. The solid red line denotes the response for the corresponding homogeneous model (Fig. 8). The arrow indicates the Stoneley wave.

very pronounced and its sensitivity to formation permeability is correspondingly weak.

Formation heterogeneity affects the seismic wavefield primarily by scattering and associated mode conversion. This phenomenon is strongly dependent on the ratio of the prevailing wavelength and the scale of the heterogeneity as well as the standard deviation of the latter. While corresponding effects in the considered example are moderate, it still nicely illustrates the contribution of this process to the overall complexity of the recorded signal. The seismograms for the heterogeneous formation are shown in Fig. 10 and compared to the seismogram of a homogeneous formation. The amplitudes and phases between the seismograms resulting from the heterogeneous and the homogeneous formations agree reasonably well, although the scattering hampers the identification of the Stoneley wave mode.

From a practical point of view, it is important to note that our simulations demonstrate that Stoneley waves are strongly attenuated and difficult to identify at larger source–receiver offsets and that the amplitudes in the considered frequency range decay rapidly with increasing distance from the borehole wall. These observations are fully consistent with the results of earlier theoretical and experimental work by Chao *et al.* (2004). It is therefore critical to place the receivers close to the borehole wall to measure the effects outlined above.

3.3 Effects related to the presence of an excavation damage zone

Drilling inherently induces mechanical disturbances in the rocks surrounding the borehole. As a result these so-called excavation damage zones are generally associated with significantly increased porosities and permeabilities as well as weakened mechanical strength compared to the corresponding pristine formation. A number of other processes related to the construction of a borehole may also contribute to this excavation damage zone, such as, for example, the installation of a casing, which requires the drill string to be slightly larger than the diameter of the casing. This in turn results in a gap between the casing and the formation, which is usually filled with sand, cuttings and/or cement. Due to the narrow and/or irregular nature of the void space, this filling may be incomplete (e.g. Yearsley *et al.* 1991; Wheaton & Bohman 1999; Christman
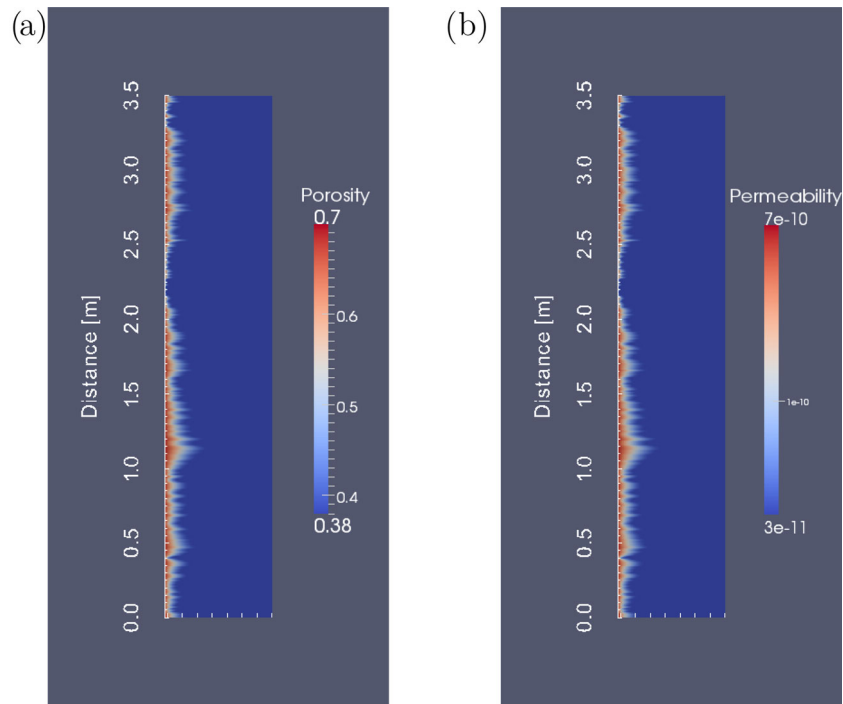
Figure 11. Rotationally invariant (a) porosity and (b) corresponding permeability models for an excavation damage zone.

et al. 2007). Similar problems exist for the so-called sand-screened completion of boreholes (e.g. Bakulin *et al.* 2008). Drilling-induced disturbances tend to be particularly pronounced and laterally extensive in soft formations and their influence on borehole measurements is widely acknowledged as being important, albeit largely unknown in detail.

In the following, we consider a canonical model to explore some first-order effects of excavation damage zones on sonic log measurements in surficial boreholes. To this end, we characterize the excavation damage zone as a region of high and spatially variable porosity and assume the seismic model to be homogeneous outside the disturbed zone and characterized by the material properties of unconsolidated sand (Table 1). As Biot's model of wave propagation in porous media does not automatically converge to wave propagation in acoustic media for high porosities, we have to consider appropriate values of the bulk and shear moduli for the highly unconsolidated sediments. Laboratory measurements of sand-screened deep-water completions and studies of unconsolidated sediments indicate that the shear modulus is small but not negligible for such materials (Bakulin *et al.* 2009; Sidler & Holliger 2010). For the purpose of this study, this implies that a porous medium model should be used rather than a suspension model that does not support shear waves.

To represent the excavation damage zone in our model, we start with a maximum porosity of 70 per cent at the first gridpoint outside the casing and gradually decrease the porosity with increasing lateral distance from the casing to the value of the homogeneous formation outside the excavation damage zone by following a Hanning taper. We assume the width of the excavation damage zone to vary with depth and introduce a 1-D stochastic variable to define the length of the Hanning taper. The mean width and standard deviation of the excavation damage zone are chosen to be 10 and 5 cm, respectively. The corresponding porosity and associated permeability (eq. C2) models are shown in Fig. 11. To account for the

above-mentioned change in the bulk and shear moduli, we use the Krief equations (eq. C3). Even though the accuracy of these empirical relations is likely to be limited for such high porosities, we do indeed obtain very small shear and bulk moduli in the immediate vicinity of the casing that we consider to be reasonable first-order approximations for exploring some of the key effects related to the presence of excavation damage zones.

For the numerical model, we use 13, 9 and 55 gridpoints along the radial direction for the acoustic and the two poroelastic domains and 351 gridpoints in the vertical direction. The ring source at the inner boundary of the acoustic domain is assumed to have the time history of a Ricker wavelet with a central frequency of 9 kHz. We evaluate 5×10^5 time steps with a discretization interval of 5×10^{-9} s.

The seismograms are recorded at the inner wall of the casing at a vertical distance of 0.75 m from the source and compared to a homogeneous reference model without an excavation damage zone (Fig. 12). The key characteristics of the seismograms observed in the presence of an excavation damage zone are the high amplitude of the fluid wave and the oscillatory wave train later in the record. Both of these features are related to the mechanical decoupling of the casing from the surrounding formation. The high amplitude of the fluid wave is a consequence of the larger effective diameter of the borehole as the casing does not constitute a strong barrier for the propagating wave, which in turn leads to substantially lower attenuation of the fluid wave (Hsui & Toksöz 1986; Norris 1989). The "ringy" wave train corresponds to surface waves travelling along the weakly connected, and hence essentially freely oscillating, casing.

To isolate the effects related to the spatial variability of this excavation damage zone, we compare the seismogram resulting from the heterogeneous excavation damage zone discussed earlier to a model characterized by a corresponding damage zone with a uniform width of ~10 cm (Fig. 12). The corresponding seismograms are indeed very similar to those obtained for corresponding excavation damage
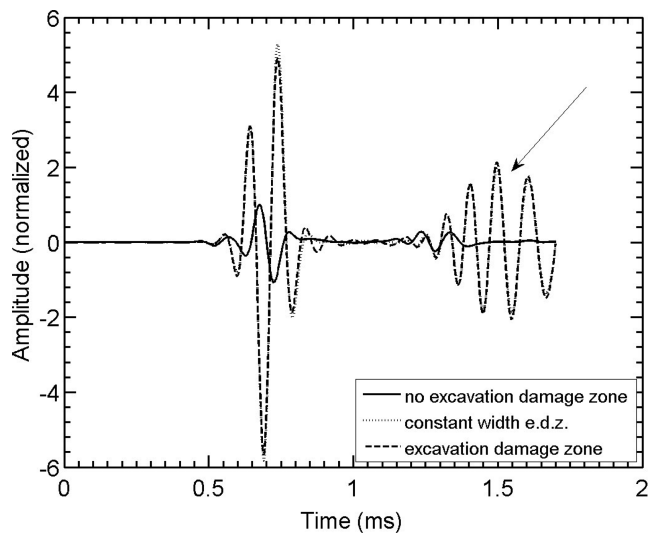
Figure 12. Seismograms showing the effect of an excavation damage zone behind a screened casing. The seismograms are recorded at the casing at a vertical distance of 0.75 m from the source. The solid black line shows the seismogram without an excavation damage zone, the dotted line corresponds to an excavation damage zone with a constant width and the dashed line to the model of an excavation damage zone characterized by the porosity shown in Fig. 11. Permeability, tortuosity, bulk and shear modulus are inferred from the porosity based on the relations given in Appendix C2. The arrow denotes the wave train bound to the casing.
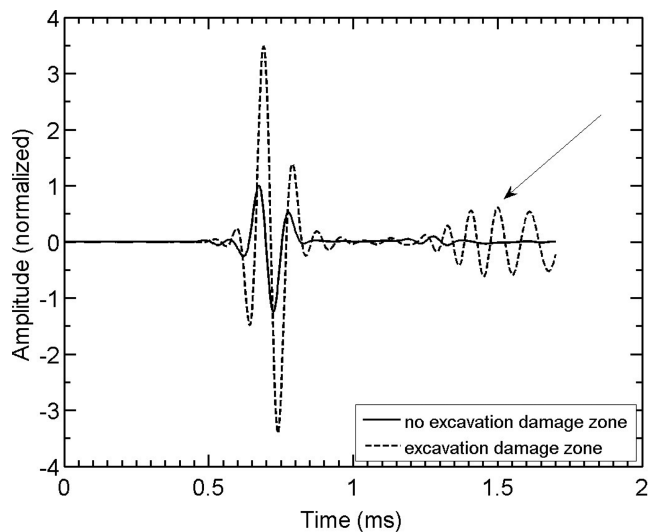

Figure 13. Same as Fig. 12, but for a borehole with a casing that is not screened.

zones characterized by a stochastically variable width. This in turn indicates that the dominant effects of the excavation damage zone are related to its characteristic mechanical and hydraulic properties, while the additional heterogeneity associated with such zones is of minor importance.

For completeness, Fig. 13 shows the corresponding simulation for an unscreened casing, that is remarkably similar to those for the screened casing (Fig. 12). Our results therefore indicate that for typical surficial borehole environments, the seismic response of an excavation damage zone clearly dominates over that of the pristine formation.

4 CONCLUSIONS

We have developed a pseudospectral numerical solution of the poroelastic equations in 3-D cylindrical coordinates and applied it to explore the propagation of seismic waves in complex borehole environments. Using a domain decomposition technique permits us to decompose the mesh into concentric subdomains. The interfaces between the various subdomains are matched by using the method of characteristics to satisfy the physical boundary conditions. This wavefield decomposition allows for an accurate modelling of interfaces and enhances the computational efficiency due to the possibility of varying the number of gridpoints in the azimuthal direction. A coordinate transformation is applied in the directions where Chebyshev operators are used in order to enlarge the inherently small grid spacing towards the edges of the computational domain. This transformation can also be used to account for variations in the borehole diameter along the borehole axis. We have applied the method to compare wave propagation in 3-D heterogeneous models with azimuthally invariant models, to estimate the sensitivity of sonic experiments to formation permeability in the presence or absence of a screened or unscreened casing, and to asses the effects of excavation damage zones. Our key findings are the following:

(i) Phases and amplitudes of the direct wave for a 3-D heterogeneous medium largely correspond to those of a corresponding rotationally invariant medium, whereas the corresponding solutions tend to differ for later arrivals, notably for the Stoneley wave. These differences increase with increasing heterogeneity and increasing source–receiver offsets.

(ii) Comparing otherwise identical simulations for viscous and non-viscous pore fluids allows for estimating the sensitivity of Stoneley waves to permeability. This sensitivity is high as long as the permeability of the casing is at least as large as that of the formation, but largely vanishes in the presence of an impermeable, unscreened casing. Conversely, the heterogeneity of the formation has a rather minor influence on the sensitivity of the Stoneley wave to permeability in cased boreholes.

(iii) The presence of an excavation damage zone largely dominates the borehole seismic response. Excavation damage zones can therefore be easily detected, but also tend to largely obliterate the response of the pristine formation.

ACKNOWLEDGEMENTS

REFERENCES

Atkinson, K.E., 1989. *An Introduction to Numerical Analysis,* 2nd edn, John Wiley and Sons.

Ávila-Carrera, R., Spurlin, J.H. & Valle-Molina, C., 2011. Simulating elastic wave propagation in boreholes: fundamentals of seismic response and quantitative interpretation of well log data, *Geophfís. Int.,* **50,** 57–76.

Bakulin, A., Sidorov, A., Kashtan, B. & Jaaskelainen, M., 2008. Real-time completion monitoring with acoustic waves, *Geophysics,* **73,** E15–E33.

Bakulin, A., Alexandrov, D., Sidorov, A. & Kashtan, B., 2009. Acoustic waves in sand-screened deepwater completions: comparison of experiments and modeling, *Geophysics,* **74,** E45–E56.

Baron, L. & Holliger, K., 2011. Constraints on the permeability structure of alluvial aquifers from the poro-elastic inversion of multifrequency P-wave sonic velocity logs, *IEEE Trans. Geosci. Remote Sens.,* **49,** 1937–1948.

Barrash, W., Clemo, T., Fox, J.J. & Johnson, T.C., 2006. Field, laboratory, and modeling investigation of the skin effect at wells with slotted casing, Boise Hydrogeophysical Research Site, *J. Hydrol.,* **326,** 181–198.

Berryman, J.G., 1980. Confirmation of Biot's theory, *Appl. Phys. Lett.,* **37,** 382–384.

Biot, M.A., 1956. Theory of propagation of elastic waves in a fluid-saturated porous solid. I. Low-frequency range, *J. acoust. Soc. Am.,* **28,** 168–178.

Biot, M.A., 1962. Generalized theory of acoustic propagation in porous dissipative media, *J. acoust. Soc. Am.,* **34,** 1254–1264.

Boyd, J.P., 2001. *Chebyshev and Fourier Spectral Methods,* 2nd edn, Dover Press.

Carcione, J.M., 1991. Domain decomposition for wave propagation problems, *J. Sci. Comput.,* **6,** 453–472.

Carcione, J.M., 2007. *Wave Fields in Real Media: Wave Propagation in Anisotropic, Anelastic, Porous and Electromagnetic Media,* 2nd edn, Elsevier.

Carcione, J.M. & Kosloff, D., 2013. Representation of matched-layer kernels with viscoelastic mechanical models, *Int. J. Numer. Anal. Model.,* **10,** 221–232.

Carcione, J.M. & Picotti, S., 2006. P-wave seismic attenuation by slow-wave diffusion: effects of inhomogeneous rock properties, *Geophysics,* **71,** O1–O8.

Carcione, J.M. & Poletto, F., 2008. Synthetic logs of multipole sources in boreholes based on the Kelvin–Voigt stress–strain relation, *Geophys. J. Int.,* **174,** 808–814.

Carcione, J.M., Herman, G. & ten Kroode, F. P.E., 2002. Seismic modeling, *Geophysics,* **67,** 1304–1325.

Carcione, J.M., Poletto, F. & Farina, B., 2008. Simulation of axis-symmetric seismic waves in fluid-filled boreholes in the presence of a drill string, *Comput. Geosci.,* **12,** 593–604.

Chao, G., Smeulders, D.M.J. & van Dongen, M.E.H., 2004. Shock-induced borehole waves in porous formations: theory and experiments, *J. acoust. Soc. Am.,* **116,** 693–702.

Cheng, C., Zhang, J. & Burns, D.R., 1987. Effects of in-situ permeability on the propagation of Stoneley (tube) waves in a borehole, *Geophysics,* **52,** 1279–1289.

Christakos, G., 1992. *Random Field Models in Earth Sciences,* Academic Press.

Christman, M.C., Benson, C.H. & Edil, T.B., 2007. Geophysical study of annular well seals, *Ground Water Monit. Remed.,* **22**(3), 104–112.

Clark, S.K., 1956. Torsional wave propagation in hollow cylindrical bars, *J. acoust. Soc. Am.,* **28,** 1163–1165.

Cui, Z.-W., Liu, J.-X. & Wang, K.-X., 2003. Elastic waves in non-Newtonian (Maxwell) fluid-saturated porous media, *Waves Random Media,* **13,** 191–203.

Deresiewicz, H. & Skalak, R., 1963. On uniqueness in dynamic poroelasticity, *Bull. seism. Soc. Am.,* **53,** 783–788.

Fornberg, B., 1988. The pseudospectral method: accurate representation of interfaces in elastic wave calculations, *Geophysics,* **53,** 625–637.

Fornberg, B., 1996. *A Practical Guide to Pseudospectral Methods,* Cambridge Univ. Press.

Garat, J., Krief, M., Stellingwerff, J. & Ventre, J., 1990. A petrophysical interpretation using the velocities of P and S waves (full waveform sonic), *Log Analyst.,* **31,** 355–369.

Goff, J.A. & Jordan, T.H., 1988. Stochastic modeling of seafloor morphology: inversion of sea beam data for second-order statistics, *J. geophys. Res.,* **93**(B11), 13 589–13 608.

Gottlieb, D., Gunzburger, M. & Turkel, E., 1982. On numerical boundary treatment of hyperbolic systems for finite difference and finite element methods, *SIAM J. Numer. Anal.,* **19,** 671–682.

Guan, W., Hu, H. & He, X., 2009. Finite-difference modeling of the monopole acoustic logs in a horizontally stratified porous formation, *J. acoust. Soc. Am.,* **125,** 1942–1950.

Haldorsen, J.B., Johnson, D.L., Plona, T., Sinha, B., Valero, H.-P. & Winkler, K., 2006. Borehole acoustic waves, *Oilfield Rev.,* **18,** 34–43.

Holliger, K. & Goff, J.A., 2003. A generic model for the 1/f-scaling nature of seismic velocity fluctuations, in *Heterogenity in the Crust and Upper Mantle: Nature, Scaling and Seismic Properties,* pp. 131–154, eds Goff, J. A. & Holliger, K., Kluwer.

Hsui, A.T. & Toksöz, M., 1986. Application of an acoustic model to determine in situ permeability of a borehole, *J. acoust. Soc. Am.,* **79,** 2055–2059.

Jackson, D.R. & Richardson, M.D., 2007. *High-Frequency Seafloor Acoustics,* Springer.

von Kármán, T., 1948. Progress in the statistical theory of turbulence, *J. Maritime Res.,* **7,** 252–264.

Karpfinger, F., Valero, H.-P., Gurevich, B., Bakulin, A. & Sinha, B., 2010. Spectral-method algorithm for modeling dispersion of acoustic modes in elastic cylindrical structures, *Geophysics,* **75,** H19–H27.

Käser, M., Pelties, C. & Castro, C.E., 2010. Wavefield modeling in exploration seismology using the discontinuous Galerkin finite-element method on HPC infrastructure, *Leading Edge,* **29,** 76–85.

Kessler, D. & Kosloff, D., 1991. Elastic wave propagation using cylindrical coordinates, *Geophysics,* **56,** 2080–2089.

Klimentos, T. & McCann, C., 1990. Relationships among compressional wave attenuation, porosity, clay content, and permeability in sandstones, *Geophysics,* **55**(8), 998–1014.

Lin, L., Peterson, M.L., Greenberg, A.R. & McCool, B.A., 2009. In situ measurement of permeability, *J. acoust. Soc. Am.,* **125,** EL123–EL128.

Liu, X., Greenhalgh, S. & Wang, Y., 2011. 2.5-D poroelastic wave modelling in double porosity media, *Geophys. J. Int.,* **186,** 1285–1294.

Mandelbrot, B.B., 1983. *The Fractal Geometry of Nature/Revised and Enlarged Edition,* Freeman and Co.

Mavko, G., Mukerji, T. & Dvorkin, J., 1998. *The Rock Physics Handbook: Tools for Seismic Analysis in Porous Media,* Cambridge Univ. Press.

Norris, A.N., 1989. Stoneley-wave attenuation and dispersion in permeable formations, *Geophysics,* **54,** 330–341.

Norris, A.N., 1990. The speed of a tube wave, *J. acoust. Soc. Am.,* **87,** 414–417.

Parra, J., Hackert, C., Xu, P.-C. & Collier, H.A., 2006. Attenuation analysis of acoustic waveforms in a borehole intercepted by a sand-shale sequence reservoir, *Leading Edge,* **25,** 186–193.

Qobi, L., de Kuijper, A., Tang, X.M. & Strauss, J., 2001. Permeability determination from Stoneley waves in the Ara group carbonates, Oman, *GeoArabia,* **6,** 649–666.

Randall, C., 1991. Multipole acoustic waveforms in nonaxisymmetric boreholes and formations, *J. acoust. Soc. Am.,* **90,** 1620–1631.

Randall, C.J., Scheibner, D.J. & Wu, P., 1991. Multipole borehole acoustic waveforms: synthetic logs with beds and borehole washouts, *Geophysics,* **56,** 1757–1769.

Rosenbaum, J.H., 1974. Synthetic microseismograms: logging in porous formations, *Geophysics,* **39,** 14–32.

Sidler, R. & Holliger, K., 2005. Kriging of scale-invariant data: optimal parameterization of the autocovariance model, in *Geostatistics for Environmental Applications,* pp. 63–74, eds Renard, P., Demougeot-Renard, H. & Froidevaux, R., Springer.

Sidler, R. & Holliger, K., 2010. Seismic reflectivity of the sediment-covered seafloor: effects of velocity gradients and fine-scale layering, *Geophys. J. Int.,* **181,** 521–531.

Sidler, R., Carcione, J.M. & Holliger, K., 2010. Simulation of surface waves in porous media, *Geophys. J. Int.,* **183,** 820–832.

Sidler, R., Carcione, J.M. & Holliger, K., 2013. A pseudo-spectral method for the simulation of poro-elastic seismic wave propagation in 2D polar coordinates using domain decomposition, *J. Comput. Phys.,* **235,** 846–864.

Tang, X.M. & Cheng, C.H., 1993. The effect of a logging tool on the Stoneley wave propagation in elastic and porous formation, *Log Analyst.,* **34,** 46–56.

Tang, X. & Cheng, C. H.A., 1996. Fast inversion of formation permeability from Stoneley wave logs using a simplified Biot-Rosenbaum model, *Geophysics,* **61,** 639–645.

Tang, X.M. & Cheng, A., 2004. *Quantitative Borehole Acoustic Methods, Handbook of Geophysical Exploration,* Elsevier.

Tessmer, E., Kessler, D., Kosloff, D. & Behle, A., 1992. Multi-domain Chebyshev-Fourier method for the solution of the equations of motion of dynamic elasticity, *J. Comput. Phys.,* **100,** 355–363.

Tsang, L. & Rader, D., 1979. Numerical evaluation of the transient acoustic waveform due to a point source in a fluid-filled borehole, *Geophysics,* **44,** 1706–1720.

Wheaton, J. & Bohman, B., 1999. Geophysical investigations of cased well completions, *Ground Water Monit. Remed.,* **19,** 143–151.

White, J.E., 1965. *Seismic Waves: Radiation, Transmission, and Attenuation,* McGraw-Hill.

White, J.E. & Zechman, R.E., 1968. Computed response of an acoustic logging tool, *Geophysics,* **33,** 302–310.

Winkler, K.W., Liu, H.-L. & Johnson, D.L., 1989. Permeability and borehole Stoneley waves: comparison between experiment and theory, *Geophysics,* **54,** 66–75.

Yearsley, E.N., Crowder, R. & Irons, L., 1991. Monitoring well completion evaluation with borehole geophysical density logging, *Ground Water Monit. Remed.,* **11,** 103–111.

APPENDIX A: LIST OF SYMBOLS

Grain bulk modulus	K_s	Fluid displacement vector	**U**
Grain shear modulus	μ_s	Solid displacement vector	**u**
Grain density	ρ_s	Relative fluid displacement	**u**$_f$
Frame bulk modulus	K_m	Particle velocity vector	**v**
Frame shear modulus	μ	Relative fluid velocity vector	**q**
Porosity	ϕ	Stress tensor	τ
Frame permeability	κ	Pore fluid pressure	p
Tortuosity	$\mathcal{T}$	Bulk density	ρ
Pore fluid density	ρ_f	Effective stress coefficient	α
Fluid storage coefficient	M	Pore fluid bulk modulus	K_f
Pore fluid viscosity	η	polar number	m
Acoustic particle velocity vector	**w**	Acoustic pressure	p_a
Acoustic bulk modulus	K_a	Acoustic impedance	I_f
Acoustic density	ρ_a		

APPENDIX B: BOUNDARY CONDITIONS

To obtain the characteristic vector for a 3-D poroelastic medium in cylindrical coordinates, we recast the regular part ($\eta = 0$) of eqs (12)–(25) as (Sidler *et al.* 2013)

$$\mathbf{H}\mathbf{v}_{,t} = \mathbf{A}\mathbf{v}_{,r} + \mathbf{B}\mathbf{v}_{,\theta} + \mathbf{C}\mathbf{v}_{,z}, \tag{B1}$$

where **H**, **A**, **B** and **C** are matrices containing the material properties and

$$\mathbf{v} = [v_r, v_\theta, v_z, q_r, q_\theta, q_z, \tau_{rr}, \tau_{\theta\theta}, \tau_{zz}, \tau_{r\theta}, \tau_{rz}, \tau_{z\theta}, p]^\top, \tag{B2}$$

is the field vector. The relevant matrix to implement the boundary conditions at the boundaries perpendicular to the *r*-direction is

$$\mathbf{A} = \begin{pmatrix}
0 & 0 & 0 & 0 & 0 & 0 & \gamma_{11} & 0 & 0 & 0 & 0 & 0 & \gamma_{12} \\
0 & 0 & 0 & 0 & 0 & 0 & 0 & 0 & 0 & \gamma_{11} & 0 & 0 & 0 \\
0 & 0 & 0 & 0 & 0 & 0 & 0 & 0 & 0 & 0 & \gamma_{11} & 0 & 0 \\
0 & 0 & 0 & 0 & 0 & 0 & -\gamma_{12} & 0 & 0 & 0 & 0 & 0 & \gamma_{22} \\
0 & 0 & 0 & 0 & 0 & 0 & 0 & 0 & 0 & -\gamma_{12} & 0 & 0 & 0 \\
0 & 0 & 0 & 0 & 0 & 0 & 0 & 0 & 0 & 0 & -\gamma_{12} & 0 & 0 \\
E_m + \alpha^2 M & 0 & 0 & \alpha M & 0 & 0 & 0 & 0 & 0 & 0 & 0 & 0 & 0 \\
E_m + \alpha^2 M - 2\mu & 0 & 0 & \alpha M & 0 & 0 & 0 & 0 & 0 & 0 & 0 & 0 & 0 \\
E_m + \alpha^2 M - 2\mu & 0 & 0 & \alpha M & 0 & 0 & 0 & 0 & 0 & 0 & 0 & 0 & 0 \\
0 & \mu & 0 & 0 & 0 & 0 & 0 & 0 & 0 & 0 & 0 & 0 & 0 \\
0 & 0 & \mu & 0 & 0 & 0 & 0 & 0 & 0 & 0 & 0 & 0 & 0 \\
0 & 0 & 0 & 0 & 0 & 0 & 0 & 0 & 0 & 0 & 0 & 0 & 0 \\
-\alpha M & 0 & 0 & -M & 0 & 0 & 0 & 0 & 0 & 0 & 0 & 0 & 0
\end{pmatrix}. \tag{B3}$$

The characteristic vector is given by

$$\mathbf{c} = \mathbf{L}\mathbf{v}, \tag{B4}$$

where **L** is the matrix whose rows are the left eigenvectors of matrix **A**. Vector **c** satisfies

$$\dot{\mathbf{c}} = \mathbf{\Lambda}\mathbf{c}_{,r},$$ (B5)

where the diagonal matrix $\mathbf{\Lambda}$ is given by

$$\mathbf{\Lambda} = \mathbf{L}\mathbf{A}\mathbf{L}^{-1}.$$ (B6)

The 13 eigenvalues, that is, the elements of $\mathbf{\Lambda}$, are given by

$$0; \; 0; \; 0; \; 0; \; 0; \; \pm V_{\pm}; \; \pm\sqrt{\gamma_{11}\mu}; \; \pm\sqrt{\gamma_{11}\mu},$$ (B7)

where

$$V_{\pm} = \sqrt{\frac{b \pm c}{2}},$$ (B8)

and

$$b = E_{\mathrm{G}}\gamma_{11} - 2M\alpha\gamma_{12} - M\gamma_{22},$$ (B9)

with

$$E_{\mathrm{G}} = E_{\mathrm{m}} + \alpha^2 M$$ (B10)

denoting the Gassmann P wave modulus E_{G}. The scalar c, not to be confused with the characteristic vector $\mathbf{c}$, satisfies

$$b^2 - c^2 = 4M\left(M\alpha^2 - E_{\mathrm{G}}\right)\left(\gamma_{12}^2 + \gamma_{11}\gamma_{22}\right).$$ (B11)

The non-zero eigenvalues are the velocities of the ingoing and outgoing waves. The third set of eigenvalues corresponds to the fast and slow P waves, as defined by the plus and minus signs inside the square root, respectively. Then follow the four eigenvalues corresponding to the ingoing and outgoing S waves. The matrix $\mathbf{L}$ is given by

$$\mathbf{L}^{-1} = \begin{pmatrix} 0 & 0 & 0 & 0 & 0 & 0 & 0 & 0 & 0 & 0 & 0 & 1 & 0 \\ 0 & 0 & 0 & 0 & 0 & 0 & l_{27} & 0 & 1 & 0 & 0 & 0 & l_{213} \\ 0 & 0 & 0 & 0 & 0 & 0 & l_{27} & 1 & 0 & 0 & 0 & 0 & l_{213} \\ 0 & 0 & l_{43} & 0 & 0 & 1 & 0 & 0 & 0 & 0 & 0 & 0 & 0 \\ 0 & l_{43} & 0 & 0 & 1 & 0 & 0 & 0 & 0 & 0 & 0 & 0 & 0 \\ l_{61} & 0 & 0 & l_{64} & 0 & 0 & l_{67} & 0 & 0 & 0 & 0 & 0 & l_{613} \\ -l_{61} & 0 & 0 & -l_{64} & 0 & 0 & l_{67} & 0 & 0 & 0 & 0 & 0 & l_{613} \\ l_{81} & 0 & 0 & l_{84} & 0 & 0 & -l_{67} & 0 & 0 & 0 & 0 & 0 & l_{813} \\ -l_{81} & 0 & 0 & -l_{84} & 0 & 0 & -l_{67} & 0 & 0 & 0 & 0 & 0 & l_{813} \\ 0 & 0 & l_{103} & 0 & 0 & 0 & 0 & 0 & 0 & 0 & 1/2 & 0 & 0 \\ 0 & l_{103} & 0 & 0 & 0 & 0 & 0 & 0 & 0 & 1/2 & 0 & 0 & 0 \\ 0 & 0 & -l_{103} & 0 & 0 & 0 & 0 & 0 & 0 & 0 & 1/2 & 0 & 0 \\ 0 & -l_{103} & 0 & 0 & 0 & 0 & 0 & 0 & 0 & 1/2 & 0 & 0 & 0 \end{pmatrix},$$ (B12)

where

$$l_{43} = \frac{\gamma_{12}}{\gamma_{11}}, \quad l_{103} = -\frac{1}{2}\sqrt{\frac{\mu}{\gamma_{11}}},$$ (B13)

$$l_{27} = \frac{2eM}{V_{+}^2(c-b)}\left(M\alpha^2 - E_{\mathrm{G}} + 2\mu\right),$$ (B14)

$$l_{213} = \frac{4eM\alpha\mu}{V_{+}^2(c-b)},$$ (B15)

$$l_{61} = -\frac{V_{-}}{4ce}\left(2M\alpha\gamma_{11}\gamma_{22} + \gamma_{12}(c + E_{\mathrm{G}}\gamma_{11} - M\gamma_{22})\right),$$ (B16)

$$l_{64} = -\frac{V_{-}}{4ce}\left(E_{\mathrm{G}}\gamma_{11}^2 + (c - 2M\alpha\gamma_{12} + M\gamma_{22})\gamma_{11} + 2M\gamma_{12}^2\right),$$ (B17)

$$l_{67} = \frac{M}{2c}\left(\alpha\gamma_{11} - \gamma_{12}\right),$$ (B18)

$$l_{81} = -\frac{V_+}{4ce}\left(\gamma_{12}(c - E_G\gamma_{11} + M\gamma_{22}) - 2M\alpha\gamma_{11}\gamma_{22}\right),$$
(B19)

$$l_{84} = -\frac{V_+}{4ce}\left(-E_G\gamma_{11}^2 + (c + 2M\alpha\gamma_{12} - M\gamma_{22})\gamma_{11} - 2M\gamma_{12}^2\right),$$
(B20)

$$l_{613} = \frac{c + E_G\gamma_{11} + M\gamma_{22}}{4c},$$
(B21)

$$l_{813} = \frac{c - E_G\gamma_{11} - M\gamma_{22}}{4c},$$
(B22)

with

$$e = \gamma_{12}^2 + \gamma_{11}\gamma_{22}.$$
(B23)

Hence, the characteristic vector (B4) is given by

$$\mathbf{c} = \begin{pmatrix} c_1 \\ c_2^{(old)} \\ c_3^{(old)} \\ c_4^{(old)} \\ c_5^{(old)} \\ c_6^{(old)} \\ c_7^{(old)} \\ c_8^{(old)} \\ c_9^{(old)} \\ c_{10}^{(old)} \\ c_{11}^{(old)} \\ c_{12}^{(old)} \\ c_{13}^{(old)} \end{pmatrix} = \begin{pmatrix} \tau_{z\theta} \\ l_{27}\tau_{rr} + \tau_{zz} + l_{213}p \\ l_{27}\tau_{rr} + \tau_{\theta\theta} + l_{213}p \\ l_{43}v_z + q_z \\ l_{43}v_\theta + q_\theta \\ l_{61}v_r + l_{64}q_r + l_{67}\tau_{rr} + l_{613}p \\ -l_{61}v_r - l_{64}q_r + l_{67}\tau_{rr} + l_{613}p \\ l_{81}v_r + l_{84}q_r - l_{67}\tau_{rr} + l_{813}p \\ -l_{81}v_r - l_{84}q_r - l_{67}\tau_{rr} + l_{813}p \\ l_{103}v_z + \tau_{rz}/2 \\ l_{103}v_\theta + \tau_{r\theta}/2 \\ -l_{103}v_z + \tau_{rz}/2 \\ -l_{103}v_\theta + \tau_{r\theta}/2 \end{pmatrix}.$$
(B24)

It can be shown that the first five rows are the zero-eigenvalue characteristics, the sixth and seventh row correspond to the slow P waves, the eighth and ninth row to the fast P waves and the 10th–13th row to the in- and outgoing S waves, respectively.

Let us now consider the same approach for the acoustic equations of motion in the fluid domain (28) and (29). It is easy to show that the characteristics vector corresponding to the unknown vector $(w_r, w_\theta, w_z, p_a)^\top$ and the matrix

$$\mathbf{A} = \begin{pmatrix} 0 & 0 & 0 & \rho_a^{-1} \\ 0 & 0 & 0 & 0 \\ 0 & 0 & 0 & 0 \\ K_a & 0 & 0 & 0 \end{pmatrix}$$
(B25)

is

$$\mathbf{d} = \begin{pmatrix} d_1 \\ d_2 \\ d_3 \\ d_4 \end{pmatrix} = \frac{1}{2}\begin{pmatrix} 2w_z \\ 2w_\theta \\ p_a - I_f w_r \\ p_a + I_f w_r \end{pmatrix},$$
(B26)

where d_1 and d_2 are the characteristic in the vertical and azimuthal direction, while d_2 and d_3 are the inward and outward characteristics along the radial direction, respectively, and $I_f = \sqrt{\rho_a K_a}$ is the fluid impedance (Sidler *et al.* 2010).

B1 Rigid boundary conditions for an acoustic domain

The rigid boundary conditions at the centre of the fluid-filled domain are

$$w_r = 0, \quad w_\theta^{new} = w_\theta^{old}, \quad w_z^{new} = w_z^{old}.$$
(B27)

Additionally the characteristic for the inward travelling wave is retained. Thus, the field variables at this boundary have to be updated as

$$w_r^{(\text{new})} = 0,$$
$$w_\theta^{(\text{new})} = w_\theta^{(\text{old})},$$
$$w_z^{(\text{new})} = w_z^{(\text{old})},$$
$$p_a^{(\text{new})} = 2d_3^{(\text{old})}, \tag{B28}$$

with the characteristic for the inward travelling wave

$$d_3 = \frac{1}{2}(p_a - I_f w_r). \tag{B29}$$

B2 Fluid/porous-solid boundary conditions

Let us denote by p_a and p the pressure in the fluid and porous medium domains, respectively. The boundary conditions at an interface between a porous medium and a fluid are

$$q_r + v_r = w_r, \quad p_a - p = Tq_r, \quad \tau_{rr} = p_a, \quad \tau_{r\theta} = 0, \quad \tau_{rz} = 0, \tag{B30}$$

where T is the dimensionless surface flow impedance. $T = 0$ corresponds to the open-pore case, whereas $T = \infty$ corresponds to the closed-pore case. The field variables are updated as

$$v_r^{(\text{new})}D = c_8^{(\text{old})}\left(-l_{64} + I_f l_{67} + (I_f + T)l_{613}\right) + c_6^{(\text{old})}\left(I_f l_{67} + l_{84} - (I_f + T)l_{813}\right) + 2d_3^{(\text{old})}\left(-l_{67}\left(l_{64} + l_{84}\right) + (Tl_{67} - l_{84})l_{613}\right.$$
$$\left. + (l_{64} + Tl_{67})l_{813}\right),$$

$$v_\theta^{(\text{new})} = c_{11}^{(\text{old})}/l_{103},$$

$$v_z^{(\text{new})} = c_{10}^{(\text{old})}/l_{103},$$

$$q_r^{(\text{new})}D = c_8^{(\text{old})}\left(l_{61} - I_f\left(l_{67} + l_{613}\right)\right) + 2d_3^{(\text{old})}\left(l_{81}\left(l_{67} + l_{613}\right) + l_{61}\left(l_{67} - l_{813}\right)\right) - c_6^{(\text{old})}\left(I_f l_{67} + l_{81} - I_f l_{813}\right),$$

$$q_\theta^{(\text{new})} = c_5^{(\text{old})} - c_{11}^{(\text{old})}l_{43}/l_{103},$$

$$q_z^{(\text{new})} = c_4^{(\text{old})} - c_{10}^{(\text{old})}l_{43}/l_{103},$$

$$\tau_{rr}^{(\text{new})}D = I_f c_8^{(\text{old})}\left(l_{61} - l_{64} + Tl_{613}\right) + I_f c_6^{(\text{old})}\left(l_{81} - l_{84} + Tl_{813}\right) + 2d_3^{(\text{old})}\left(-l_{64}l_{81} + Tl_{81}l_{613} + l_{61}\left(l_{84} - Tl_{813}\right)\right),$$

$$\tau_{\theta\theta}^{(\text{new})}D = Dc_3^{(\text{old})} + c_8^{(\text{old})}\left(\left((I_f + T)l_{61} - I_f\left(l_{64} + Tl_{67}\right)\right)l_{213} + I_f l_{27}\left(l_{61} - l_{64} + Tl_{613}\right)\right)$$
$$- c_6^{(\text{old})}\left((I_f Tl_{67} + (I_f + T)l_{81} - I_f l_{84})l_{213} + I_f l_{27}\left(l_{81} - l_{84} + Tl_{813}\right)\right) + 2d_3^{(\text{old})}[((l_{64} + Tl_{67})l_{81} + l_{61}\left(Tl_{67} - l_{84}\right))l_{213}$$
$$+ l_{27}\left(-l_{61}l_{84} + l_{81}\left(l_{64} - Tl_{613}\right) + Tl_{61}l_{813}\right)],$$

$$\tau_{zz}^{(\text{new})}D = Dc_2^{(\text{old})} + C_8^{(\text{old})}\left(\left((I_f + T)l_{61} - I_f(l_{64}) + Tl_{67}l_{213}\right) + I_f l_{27}(l_{61} - l_{64} + Tl_{613})\right)$$
$$- c_6^{(\text{old})}\left((I_f Tl_{67} + (I_f + T)l_{81} - I_f l_{84})l_{213} + I_f l_{27}(l_{81} - l_{84} + Tl_{813})\right)$$
$$+ 2d_3^{(\text{old})}[((l_{64} + Tl_{67})l_{81} + l_{61}(Tl_{67} - l_{84}))l_{213}$$
$$+ l_{27}(-l_{61}l_{84} + l_{81}(l_{64} - Tl_{613}) + Tl_{61}l_{813})],$$

$$\tau_{r\theta}^{(\text{new})} = 0,$$

$$\tau_{rz}^{(\text{new})} = 0.$$

$$p^{(\text{new})}D = c_8^{(\text{old})}\left(-(I_f + T)l_{61} + I_f\left(l_{64} + Tl_{67}\right)\right) - 2d_3^{(\text{old})}\left((l_{64} + Tl_{67})l_{81} + l_{61}\left(Tl_{67} - l_{84}\right)\right) + c_6^{(\text{old})}\left(I_f Tl_{67} + (I_f + T)l_{81} - I_f l_{84}\right), \tag{B31}$$

where

$$D = [I_f l_{67}l_{81} - I_f l_{67}l_{84} + I_f Tl_{67}l_{613} + I_f l_{81}l_{613} + Tl_{81}l_{613} - I_f l_{84}l_{613}$$
$$+ I_f Tl_{67}l_{813} - l_{64}\left(I_f l_{67} + l_{81} - I_f l_{813}\right)] + l_{61}\left(I_f l_{67} + l_{84} - (I_f + T)l_{813}\right). \tag{B32}$$

The updated fields for the fluid are

$$w_r^{(\text{new})} = v_r^{(\text{new})} + q_r^{(\text{new})},$$
$$w_\theta^{(\text{new})} = d_2^{(\text{old})},$$
$$w_z^{(\text{new})} = d_1^{(\text{old})},$$
$$p_a^{(\text{new})} = Tq_r^{(\text{new})} + p^{(\text{new})}. \tag{B33}$$

B3 Porous-solid/porous-solid open-pore boundary conditions

The open-pore boundary conditions between two porous media (1) and (2) are

$$v_r(1) = v_r(2), \quad v_\theta(1) = v_\theta(2), \quad v_z(1) = v_z(2), \quad q_r(1) = q_r(2),$$
$$\tau_{rr}(1) = \tau_{rr}(2), \quad \tau_{r\theta}(1) = \tau_{r\theta}(2), \quad \tau_{rz}(1) = \tau_{rz}(2), \quad p(1) = p(2). \tag{B34}$$

B4 Non-reflecting boundary conditions for a porous solid

The absorbing boundary conditions for the outer boundary can be obtained by retaining the outward characteristics and setting the inward characteristics $c_6^{(\text{old})}$, $c_8^{(\text{old})}$, $c_{10}^{(\text{old})}$ and $c_{12}^{(\text{old})}$ to zero. This leads to the following boundary conditions:

$$v_r^{(\text{new})} = (c_9^{(\text{old})}l_{64} - c_7^{(\text{old})}l_{84})/(-2l_{64}l_{81} + 2l_{61}l_{84}),$$

$$v_\theta^{(\text{new})} = -c_{13}^{(\text{old})}/(2l_{103}),$$

$$v_z^{(\text{new})} = -(c_{12}^{(\text{old})})/(2l_{103}),$$

$$q_r^{(\text{new})} = (c_9^{(\text{old})}l_{61} - c_7^{(\text{old})}l_{81})/(2l_{64}l_{81} - 2l_{61}l_{84}),$$

$$q_\theta^{(\text{new})} = c_5^{(\text{old})} + (c_{13}^{(\text{old})}l_{43})/(2l_{103}),$$

$$q_z^{(\text{new})} = c_4^{(\text{old})} + (c_{12}^{(\text{old})}l_{43})/(2l_{103}),$$

$$\tau_{rr}^{(\text{new})} = (-c_9^{(\text{old})}l_{613} + c_7^{(\text{old})}l_{813})/(2l_{67}(l_{613} + l_{813})),$$

$$\tau_{\theta\theta}^{(\text{new})} = [c_9^{(\text{old})}(-l_{67}l_{213} + l_{27}l_{613}) + 2c_3^{(\text{old})}l_{67}(l_{613} + l_{813})$$
$$\qquad -c_7^{(\text{old})}(l_{67}l_{213} + l_{27}l_{813})]/(2l_{67}(l_{613} + l_{813})),$$

$$\tau_{zz}^{(\text{new})} = [c_9^{(\text{old})}(-l_{67}l_{213} + l_{27}l_{613}) + 2c_2^{(\text{old})}l_{67}(l_{613} + l_{813})$$
$$\qquad -c_7^{(\text{old})}(l_{67}l_{213} + l_{27}l_{813})]/(2l_{67}(l_{613} + l_{813})),$$

$$\tau_{r\theta}^{(\text{new})} = c_{13}^{(\text{old})},$$

$$\tau_{rz}^{(\text{new})} = c_{12}^{(\text{old})},$$

$$p^{(\text{new})} = (c_7^{(\text{old})} + c_9^{(\text{old})})/(2(l_{613} + l_{813})). \tag{B35}$$

APPENDIX C: HETEROGENEOUS POROUS MEDIUM

The quantities of a heterogeneous Biot-type porous medium are not completely independent of each other and empirical relationships have been established to parametrize additional quantities from known ones (Carcione & Picotti 2006; Sidler *et al.* 2010). We therefore first create a stochastic porosity distribution, based on which we then evaluate the related parameters.

C1 Stochastic medium

To generate a band-limited fractal distribution for the porosity, we use the von Kármán auto-covariance function and the 'Wiener-Khinchine' theorem to relate it to the spectral density function of the considered stochastic distribution (von Kármán 1948; Mandelbrot 1983; Christakos 1992; Sidler & Holliger 2005). The Fourier transform of the von Kármán auto-covariance function is given by

$$P_{hh}(\vec{k}) = \frac{\sigma_{\text{h}}^2(2\sqrt{\pi a})^E \Gamma(\nu + E/2)}{\Gamma(\nu)(1 + \vec{k}^2 a^2)^{\nu + E/2}}, \tag{C1}$$

where $\vec{k}$ is the vectorial wavenumber, σ_{h} is the variance and a the correlation length. The parameter $0 \leq \nu \leq 1$ is related to the so-called Hausdorff fractal dimension H_{D} and thus to the complexity of the medium as $H_{\text{D}} = E + 1 - \nu$ (e.g. Goff & Jordan 1988), where E denotes the underlying Euclidian dimension of the stochastic process. Taking the square root yields the corresponding amplitude spectrum. The actual realization of the stochastic medium is then obtained by adding a random phase spectrum followed by the inverse Fourier transform and appropriate scaling.

C2 Empirical relationships between properties of a porous medium

A relationship between porosity and permeability based on geometrical considerations is given by the Kozeny–Carman equation (Mavko *et al.* 1998)

$$\kappa = \frac{B\phi^3 d^2}{(1 - \phi)^2}, \tag{C2}$$

where ϕ is the porosity, d is the grain diameter and $B = 0.003$ an empirical constant. Jackson & Richardson (2007) specify an average grain diameter $d = 0.25$ mm for the fine- to medium-grained marine sandy sediments.

The matrix and shear bulk moduli can be computed from the porosity and the solid grain bulk and shear modulus using the Krief equations (Garat *et al.* 1990)

$$K_{\mathrm{m}} = K_{\mathrm{s}}(1 - \phi)^{4/(1-\phi)}, \tag{C3}$$

$$\mu = \frac{K_{\mathrm{m}}}{K_{\mathrm{s}}}\mu_{\mathrm{s}}. \tag{C4}$$

The tortuosity can be estimated from the porosity as (Berryman 1980)

$$\mathcal{T} = \frac{1}{2}\left(1 + \frac{1}{\phi}\right). \tag{C5}$$

SUPPORTING INFORMATION

Additional Supporting Information may be found in the online version of this article:

(http://gji.oxfordjournals.org/lookup/suppl/doi:10.1093/gji/ggt447/-/DC1).

Please note: Oxford University Press are not responsible for the content or functionality of any supporting materials supplied by the authors. Any queries (other than missing material) should be directed to the corresponding author for the article.